Near-field Tracking with Large Antenna Arrays: Fundamental Limits and Practical Algorithms

Anna Guerra, *Member, IEEE,* Francesco Guidi, *Member, IEEE,*
Davide Dardari, *Senior, IEEE,* and Petar M. Djurić, *Fellow, IEEE,*

Abstract—**Applications towards 6G have brought a huge interest towards arrays with a high number of antennas and operating within the millimeter and sub-THz bandwidths for joint communication, sensing, and localization. With such large arrays, the plane wave approximation is often not accurate because the system may operate in the (radiating) near-field propagation region (i.e., the Fresnel region) where the electromagnetic field wavefront is spherical. In this case, the curvature of arrival (CoA) is a measure of the spherical wavefront that can be used to infer the source position using only a single large antenna array. In this paper, we study a near-field tracking problem for inferring the state (i.e., the position and velocity) of a moving source with an ad-hoc observation model that accounts for the phase-difference profile of a large receiving array. For this tracking problem, we derive the posterior Cramér-Rao Lower Bound (P-CRLB), and we provide insights on how the loss of positioning information outside the Fresnel region results from an increase of the ranging error rather than from inaccuracies of angular estimation. Then, we investigate the accuracy and complexity performance of different Bayesian tracking algorithms in the presence of model parameter mismatches and abrupt trajectory changes. Our results demonstrate the feasibility and high accuracy of most tracking approaches without the need for wideband signals and of any synchronization scheme.**

Index Terms—**Near-field tracking, posterior Cramér-Rao lower bound, curvature-of-arrival, large antenna array.**

I. INTRODUCTION

Short-range localization and tracking techniques have recently attracted great interest in all the scenarios where the signal coming from the Global Navigation Satellite System (GNSS) is denied or leads to a low-accuracy positioning [1]–[3]. Nowadays, there is a large variety of ad-hoc solutions for high-accuracy positioning, spanning from systems based on dedicated impulse radio ultrawide bandwidth (UWB) technology to system integrating heterogeneous sensors [4]. Unfortunately, most of the available solutions usually require an *ad-hoc* positioning infrastructure with multiple anchors, i.e., multiple reference sensors with known positions, that can be expensive or bulky, especially for indoor environments [5]. While it is possible, in principle, to avoid the need for infrastructure using simultaneous localization and mapping (SLAM) algorithms based on laser or camera sensors [6], it

is of interest to realize high-accuracy radio localization and tracking solutions that make use of the same network of access points (APs) already deployed for communication coverage.

With the sixth generation (6G) of cellular networks, further improvements are expected in localization and tracking. These improvements will result from the joint use of high frequencies and large arrays for both communication and localization purposes [7]–[13] (see Fig. 1). Following a trend started by the 5G cellular systems, many APs, equipped with massive arrays, are expected to play a dual functional role of communication and localization reference nodes. The large antenna arrays at each AP allow to collect a large set of measurements, thus enhancing the localization accuracy.

Usually, with such large arrays, source localization and tracking are based on the joint estimate of the angle-of-arrival (AOA) and time-of-arrival (TOA) [12]–[16], which requires a fine synchronization between the transmitter (namely, the source to be localized), and the receiver (the AP).[1] When synchronization is not guaranteed, it is not possible to retrieve any reliable positioning information about the transmitter if only one AP is involved in the process. Traditionally, time difference of arrival (TDOA) or two-way ranging approaches are used to overcome this issue [2], but they require multiple message-passing between nodes or the involvement of multiple APs with a good geometric dilution of precision (GDOP). When APs are closely located to each other and latency requirements become stringent, these approaches could fail and, therefore, new solutions are needed.

When the antenna array is large enough to capture the spherical characteristic of the incident wave, which happens when operating in the radiating near-field of the antenna array (Fresnel region),[2] a promising approach is to retrieve the source position directly from the curvature of arrival (CoA) encapsulated in the spherical wavefront impinging a single large array. A graphical representation is in Fig. 1. Note that throughout the paper, an array is considered large if the ratio between the maximum size of the array and the source-array distance, namely D/d, is such that the source is located in the Fresnel region. The CoA depends on the transmitter position and the array geometry, and, when it is used for localization or tracking purposes, it does not need any synchronization [7], [17], [18]. This concept is not new, and it has been investigated

A. Guerra (corresponding author, e-mail: anna.guerra3@unibo.it) and D. Dardari are with the WiLAB - Department of Electrical and Information Engineering "Guglielmo Marconi" - CNIT, University of Bologna, Italy. F. Guidi is with CNR-IEIIT, Italy. P. M. Djurić is with ECE, Stony Brook University, Stony Brook, NY 11794, USA. E-mail: petar.djuric@stonybrook.edu. This work has received funding from the EU's H2020 research and innovation programme under the Marie Skłodowska-Curie project AirSens (no. 793581). This paper was funded by the project "Dipartimenti di Eccellenza" - DEI.

---

[1]In this paper, the term "source" is used as a synonym of "user", "transmitter", "target", and "emitter", whereas the term "antenna array" refers to the "receiver", that can be located in the "AP".

[2]Note that, in this paper, the term "near–field" refers to the "Fresnel region", "radiating near–field", and "near–far field".

for different frequencies and architectures [19]–[23], entailing the adoption of distributed antennas [23]–[25]. In the next, we will review the literature on near–field tracking.

a) Related Works: Many localization methods for near-field sources have already been proposed in the literature as [26], [27] and references therein. In the near–field region, the wavefront shape varies nonlinearly with the array position and it is characterized by both the angular and the range parameters. Hence, it can be used for source positioning or tracking.

For example, in [28], a near-field model is used to localize multiple sources using an extended version of the MUSIC algorithm, also referred to as *spherical wave* MUSIC. In [19], an approach for direct wireless positioning with narrowband multi-tone signaling and multi-arrays is described, whereas, in [29], a MUSIC-based method with an extensive analysis on the attainable fundamental localization limits is derived for near-field propagation conditions. A detailed investigation using acoustic waveforms has been carried out in [21], [30]. More recently, [23]–[25] concern with the source localization problem by forming a large aperture array of passive sensors connected with fiber, wireless links, or wired lines. Following the same trend, [31], [32] provide an arrayed Extended Kalman Filter (EKF) approach for multiple source tracking and a comparison with the posterior Cramér-Rao Lower Bound (P-CRLB) in the lower microwave band. In [33], a multipath localization algorithm is investigated where not only the signal sources but also their multipath reflectors are localized in the radiating near–field of the antenna.

Unfortunately, these studies usually refer to acoustic waves or radiofrequency (RF) microwaves considering only very short distances or using very large, often not practical, distributed antennas. As an example, in [23], the array is composed of passive sensors distributed in the environment and spaced apart of several meters.

At millimeter-waves (mm-wave) frequencies, source positioning and tracking are in principle possible even with antenna arrays with limited aperture and for distances up to several meters [7], [12], [17], [18]. In fact, thanks to a reduced wavelength, a large number of antennas can be accommodated in a small area [34]–[36]. For example for a uniform rectangular array (URA) of 400 antennas, we have a maximum size of $0.14\,$m for a central frequency of $28\,$GHz. Therefore, the Fraunhofer distance limiting the near–field region is approximately $4\,$m. To preserve the same boundary at $2.4\,$GHz, the array size should approximately be three times larger.

Preliminary studies on near-field fundamental limits on positioning with fifth generation (5G) antenna arrays have been recently addressed in [16], [37], [38], but considering a static scenario and non-Bayesian methods. The papers in [16], [18], [39]–[43] propose some derivations valid for near–field sources in presence of synchronization between the transmitters and the receiver. In [18], [42], [43] a model valid for metasurfaces has been recently proposed for reconfigurable intelligent surface (RIS)-aided localization scenarios. None of these works deals with an asymptotic analysis to evaluate the behaviour of the spherical information as the source distance
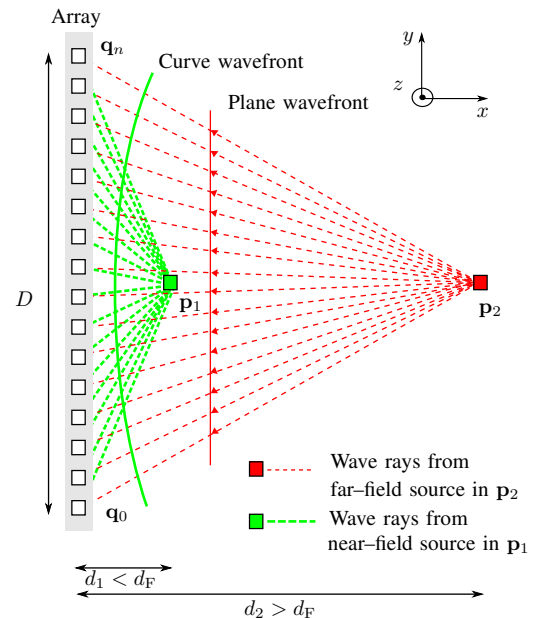

Fig. 1. Curvature of arrival of the wavefront impinging on a large array when the source is in near–field in $\mathbf{p}_1$. When instead the source is in far–field in $\mathbf{p}_2$, the wavefront can be approximated as planar.

increases compared to the maximum array size.

b) Contributions: In this paper, we investigate the fundamental limits in source tracking in a single-array scenario to highlight the behavior of position information inside and outside the Fresnel region, and we assess the accuracy and complexity performance through practical algorithms working with CoA in absence of synchronization between the array and the source. To this end, we consider a wrapped phase-difference observation model accounting for the near-field wavefronts, and we derive compact formulas for different array configurations to gain further insights on the capability to infer the position information when moving from near–field to far–field regions, conventionally delimited by the Fraunhofer distance [44]. Through an asymptotic analysis, we evaluate the role of ranging and bearing information on localization when the source-array distance increases, showing that the CoA provides both types of information only in the Fresnel region while, elsewhere, only bearing data can be correctly estimated. Further, we investigate different Bayesian tracking algorithms to assess their robustness, accuracy, and complexity in different situations.

The main contributions of the paper are as follows.

- We introduce a narrowband signal and observation model, accounting for phase difference-of-arrival at a single large co-located antenna array, that includes CoA of the impinging wavefront;
- We derive the P-CRLB to assess the ultimate performance of the CoA–based tracking in the near– and far–field regions when the considered phase-difference model is used;
- To highlight the role of the ratio between the source distance and the array size for near-field localization and tracking, we analyze the Fisher Information Matrices (FIMs) on ranging and bearing information and

their asymptotic behaviors. Moreover, we derive compact formulas for three different array geometries;

- We evaluate the performance of different Bayesian filtering approaches considering different models and parameters available at the receiver. We investigate the complexity and robustness of the tracking algorithms under model parameter mismatches, abrupt changes of direction (i.e., model mismatches), and we show the impact of movements inside and outside the Fresnel region.

c) Notation: Scalar variables, vectors and matrices are represented with lower letters, lower bold letters, and capital bold letters, respectively (e.g., x, $\mathbf{x}$, and $\mathbf{X}$, respectively). The symbols $(\cdot)^{\mathsf{T}}$, $(\cdot)^{-1}$, and $(\cdot)^{\dagger}$ represent the transpose, inverse and Moore-Penrose pseudo-inverse operators of their arguments, respectively, and $\|\cdot\|$ is the 2-norm of its argument. We use k for discrete temporal indexing, n for antenna indexing, and m for particle indexing. As an example, $x_{n,k}$, $\mathbf{x}_{n,k}$, $\mathbf{X}_{n,k}$ stand for a scalar, a vector or a matrix related to the nth antenna at the kth time instant. With $\mathbf{I}_N$ and $\mathbf{0}_N$ we represent the identity and all-zero matrices of size $N \times N$. A probability density function is denoted by $p(\cdot)$, and $\mathbb{E}\{\mathbf{x}\}$ is the expectation of a random vector $\mathbf{x}$ with respect to its distribution. With $\mathcal{N}(\mathbf{x}; \boldsymbol{\mu}, \boldsymbol{\Sigma})$ we indicate that the random vector $\mathbf{x}$ is distributed according to a Gaussian pdf with a mean vector $\boldsymbol{\mu}$ and a covariance matrix $\boldsymbol{\Sigma}$. The notation $\mathbf{x}_{a|b}$ indicates the value of a vector $\mathbf{x}$ at time instant a estimated by considering the measurements collected up to time instant b. For example, $\mathbf{x}_{k|k-1}$ is the value of $\mathbf{x}$ predicted at time instant $k-1$ for the next time instant k, whereas, once a new measurement becomes available at k, this value is updated to $\mathbf{x}_{k|k}$. $j = \sqrt{-1}$ is the imaginary unit.

d) Organisation of the paper: The rest of the paper is organized as follows. Section II provides the signal and state-space model of the tracking problem, Sections III-IV describe the fundamental limits of near–field tracking performance and present practical algorithms for source tracking, respectively. Simulation results are reported in Section V and conclusions are drawn in Section VI.

II. SIGNAL AND STATE–SPACE MODEL

We consider a tracking scenario where a single antenna array tracks a moving source by exploiting the phase profile of the received signal caused by the CoA. We denote by $\mathbf{s}_k = \left[\mathbf{p}_k^{\mathsf{T}}, \mathbf{v}_k^{\mathsf{T}}\right]^{\mathsf{T}} \in \mathbb{R}^{N_s}$ the state composed of the position and velocity Cartesian coordinates of the source at time instant k, respectively, defined by $\mathbf{p}_k = [x_k, y_k, z_k]^{\mathsf{T}} \in \mathbb{R}^3$ and $\mathbf{v}_k = [v_{\mathsf{x},k}, v_{\mathsf{y},k}, v_{\mathsf{z},k}]^{\mathsf{T}} \in \mathbb{R}^3$. Therefore, the state dimensionality is $N_s = 6$. We also consider that the array has N antennas located at $\mathbf{q}_n = [x_n, y_n, z_n]^{\mathsf{T}} \in \mathbb{R}^3$, $n = 0, \ldots, (N-1)$, with reference location $\mathbf{q}_0$.

At each time instant, the geometric relationships between the reference location and the source are given by

$$\mathbf{p}_k = \begin{bmatrix} x_k \\ y_k \\ z_k \end{bmatrix} = \begin{bmatrix} x_0 + d_k \cos(\phi_k) \sin(\theta_k) \\ y_0 + d_k \sin(\phi_k) \sin(\theta_k) \\ z_0 + d_k \cos(\theta_k) \end{bmatrix}, \quad (1)$$

with $d_k \triangleq d_{0,k} = \|\mathbf{p}_k - \mathbf{q}_0\|$, $\phi_k \triangleq \phi_{0,k} = \mathrm{atan2}(y_k - y_0, x_k - x_0)$, and $\theta_k \triangleq \theta_{0,k} = \mathrm{acos}\left(\frac{z_k - z_0}{d_k}\right)$ being
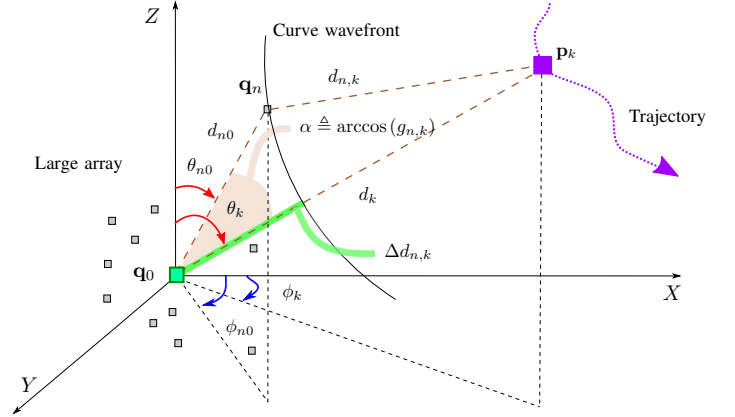

Fig. 2. Considered antenna array and system geometry. The receiver antenna array (the antennas are indicated with gray squares with reference location in $\mathbf{q}_0$ in green), tracks a moving source at $\mathbf{p}_k$ (purple square marker) whose trajectory is depicted with a dashed line.

the true distance, azimuth, and elevation angles, respectively, as represented in Fig. 2.

The collaborative source/user emits a narrowband signal such as a pilot in a resource block of an orthogonal frequency division multiplexing (OFDM) scheme centered at a frequency f_p, dedicated to positioning, which is received by the antenna array and processed for tracking purposes.[3] By considering a direct line-of-sight (LOS) link between each antenna and the source, the received signal at the nth antenna, during the pth OFDM symbol of duration T, is

$$r_n(t) = a_{n,k} \cos(2\pi f_p t - \vartheta_{n,k}) + \nu_n(t), \quad (2)$$

where $a_{n,k} \triangleq \frac{A\lambda}{4\pi d_{n,k}} \in \mathbb{R}$ and $\vartheta_{n,k} \triangleq 2\pi f_p \left(\frac{d_{n,k}}{c} + t_0\right)$ are the received signal amplitude and phase at the nth antenna of the array observed at discrete time k. The distance between the considered nth array antenna and the source is $d_{n,k}$. The received signal amplitude is $A = \sqrt{2P_t}$ with P_t being the transmitted power. The wavelength is indicated as $\lambda = \frac{c}{f_p}$, with c being the speed of light.

We assume that the source is not synchronized with the receiver so that any TOA information cannot be inferred from the signal, and the phase offset between the source and the array is not known. The unknown clock offset due to the lack of synchronization between the array and the source is t_0. Finally, $\nu_n(t)$ is the observation noise modeled as additive white Gaussian noise (AWGN) with double-sided power spectral density $\frac{N_0}{2}$.

Starting from the received signals, the sequential state estimation problem (tracking) can be formulated starting from a discrete-time state-space representation given by [45]

$$\mathbf{s}_k = \mathbf{s}_k^- + \mathbf{w}_k = \mathbf{A}_k \mathbf{s}_{k-1} + \mathbf{w}_k, \quad (3)$$

$$\mathbf{z}_k = h(\mathbf{p}_k) + \boldsymbol{\eta}_k, \quad (4)$$

where the motion model is considered a linear function of the state, with $\mathbf{s}_k^- = \mathbf{A}_k \mathbf{s}_{k-1}$ being the predicted state,

---

[3]Thanks to a proper allocation of radio resources through OFDM, the extension of this work to tracking of multiple sources is straightforward as the association problem is implicitly solved by the orthogonality of the pilot tones, and by the fact that the source is cooperative (active) with the receiver.

and $\mathbf{A}_k \in \mathbb{R}^{N_s^2}$ being the transition matrix of size $N_s \times N_s$, whereas the observation model is a nonlinear function $h : \mathbb{R}^{N_s/2} \to \mathbb{R}^N$ that will be defined in the sequel, and $\mathbf{w}_k \sim \mathcal{N}(\mathbf{w}_k; \mathbf{0}, \mathbf{Q}_k) \in \mathbb{R}^{N_s}$ and $\boldsymbol{\eta}_k \sim \mathcal{N}(\boldsymbol{\eta}_k; \mathbf{0}, \mathbf{R}_k) \in \mathbb{R}^N$ are zero-mean noise processes with $\mathbf{Q}_k$ and $\mathbf{R}_k$ being the transition and observation noise covariance matrices of sizes $N_s \times N_s$ and $N \times N$, respectively. In the next, we will assume a time invariant transition matrix and covariance matrix, e.g., $\mathbf{A}_k = \mathbf{A}$ and $\mathbf{Q}_k = \mathbf{Q}$, as well as $\mathbf{R}_k = \mathbf{R} = \sigma_\eta^2 \mathbf{I}_N$, where σ_η^2 is the variance associated to the phase-difference noise.

The observation function provides, for a given source position, the phase-differences at each antenna, i.e., the difference of phases gathered at the considered antenna and at the reference location. More specifically,

$$h(\mathbf{p}_k) = [h_0(\mathbf{p}_k), \dots, h_n(\mathbf{p}_k), \dots, h_{N-1}(\mathbf{p}_k)]^\mathsf{T}, \quad (5)$$

of size $N \times 1$, where the generic element is a phase difference between 0 and 2π, given by[4]

$$h_n(\mathbf{p}_k) = \Delta\vartheta_{n,k} \mod 2\pi, \quad (6)$$

$$\Delta\vartheta_{n,k} = \frac{2\pi}{\lambda} \Delta d_{n,k}(\mathbf{q}_n, \mathbf{p}_k), \quad (7)$$

where $\Delta\vartheta_{n,k} \triangleq \vartheta_{n,k} - \vartheta_{0,k}$ represents the difference of phases collected at locations $\mathbf{q}_n$ and at the reference location $\mathbf{q}_0$. The modulo operator is denoted with $\mod$ and returns the remainder after division (of $\Delta\vartheta_{n,k}/2\pi$) preserving the same sign of $\Delta\vartheta_{n,k}$, and $\Delta d_{n,k}(\mathbf{q}_n, \mathbf{p}_k)$ is the extra-distance traveled by the waveform to arrive to the nth antenna with respect to the reference one, represented in Fig. 2. In particular, this extra-distance is given by

$$\Delta d_{n,k}(\mathbf{q}_n, \mathbf{p}_k) = d_{n,k}(\mathbf{q}_n, \mathbf{p}_k) - d_k(\mathbf{q}_0, \mathbf{p}_k). \quad (8)$$

According to trigonometric rules, we have

$$d_{n,k}^2 = d_{n0}^2 + d_k^2 - 2 d_k d_{n0} g_{n,k}, \quad (9)$$

where $d_{n0} = \|\mathbf{q}_n - \mathbf{q}_0\|$, with $n > 0$, is the distance between the nth antenna and the reference location, and

$$g_{n,k} \triangleq g(\theta_{n0}, \phi_{n0}, \theta_k, \phi_k) = \sin(\theta_{n0}) \sin(\theta_k) \cos(\phi_{n0} - \phi_k) + \cos(\theta_{n0}) \cos(\theta_k), \quad (10)$$

is a geometric term with θ_{n0} and ϕ_{n0} being the nth antenna elevation and azimuth angles with respect to the reference location, respectively (for the reference antenna it is $\phi_{00} = \theta_{00} = 0$). Consequently, the extra-distance in (8) can be written as [7], [31]

$$\Delta d_{n,k}(\mathbf{q}_n, \mathbf{p}_k) = d_k\left(\sqrt{\mathrm{f}_{n,k}} - 1\right), \quad (11)$$

with the CoA information gathered in $\mathrm{f}_{n,k}$ as

$$\mathrm{f}_{n,k} \triangleq \mathrm{f}_{n,k}(\mathbf{q}_n, \mathbf{p}_k) = 1 + \left(\frac{d_{n0}}{d_k}\right)^2 - 2\frac{d_{n0}}{d_k} g_{n,k}. \quad (12)$$

Note that the observation function in (6) is highly nonlinear with respect to the source position as highlighted in (11)-(12). The velocity is exclusively inferred using the transition

[4]Note that the phase uncertainty due to source-array clock mismatches disappears thanks to the difference between the phases at the array antennas and the reference.

model and the latest position estimates (without measurement correction/update that only applies for position estimation) [2].

In the next sections, we will investigate the theoretical limits on source tracking as well as some practical algorithms by considering the source located both in the radiating near– and far–field regions. Conventionally, the boundary between the reactive and the radiating near–field region is $0.62\sqrt{\frac{D^3}{\lambda}}$, whereas the far–field region corresponds to distances larger than the Fraunhofer limit given by $d_\mathrm{F} \triangleq \frac{2D^2}{\lambda}$, where D is the array aperture, i.e., the largest distance between any two antennas of the array. Consequently, the radiating near–field region is [44]

$$0.62\sqrt{\frac{D^3}{\lambda}} \le d_k \le d_\mathrm{F}. \quad (13)$$

III. FUNDAMENTAL LIMITS ON NEAR–FIELD TRACKING

A. Posterior CRLB

We now derive the P-CRLB [46]–[49] for the discrete-time nonlinear problem described in this paper. As introduced in [46], [49], different Bayesian bounds can be derived depending on the choice of the probability distribution from which the Bayesian Fisher Information Matrix (FIM) is computed.

The joint distribution of the state and measurements, $p_{0:k} = p(\mathbf{s}_{0:k}, \mathbf{z}_{0:k})$, allows for the computation of the Bayesian FIM from the state history, i.e., $\mathbf{J}_{0:k}$ of size $(k+1)N_s \times (k+1)N_s$, and the derivation of the tightest P-CRLB for nonlinear filtering problems. The P-CRLB of the joint distribution can be written as the inverse of the Bayesian FIM

$$\mathbf{P}_{0:k} \ge \mathbf{J}_{0:k}^{-1}, \quad (14)$$

where $\mathbf{J}_{0:k}$ is the Bayesian FIM defined as

$$\mathbf{J}_{0:k} = \mathbb{E}_{\mathbf{s}_{0:k}, \mathbf{z}_{0:k}}\left\{\Delta_{\mathbf{s}_{0:k}}^{\mathbf{s}_{0:k}} \ln p(\mathbf{s}_{0:k}, \mathbf{z}_{0:k})\right\}, \quad (15)$$

with $\Delta_\mathbf{a}^\mathbf{b} = \nabla_\mathbf{a}^\mathsf{T} \nabla_\mathbf{b}$ and $\nabla_\mathbf{a} = \left[\frac{\partial}{\partial a_1}, \dots, \frac{\partial}{\partial a_A}\right]$ being the gradient with respect to the vector $\mathbf{a}$ of size $1 \times A$. From (15), it is possible to derive the P-CRLB on $\mathbf{s}_k$ by taking the $N_s \times N_s$ lower-right sub-matrix of the inverse of $\mathbf{J}_{0:k}$. A more elegant approach that avoids the inversion of the large FIM $\mathbf{J}_{0:k}$ is a recursive formula proposed in [46], which permits to express the FIM of $\mathbf{s}_k$, namely $\mathbf{J}_k$ of size $N_s \times N_s$, as

$$\mathbf{J}_k = \mathbf{D}_{k-1}^{22} - \mathbf{D}_{k-1}^{21}\left(\mathbf{J}_{k-1} + \mathbf{D}_{k-1}^{11}\right)^{-1}\mathbf{D}_{k-1}^{12}, \quad (16)$$

where the initial information matrix $\mathbf{J}_0 = \mathbb{E}_{\mathbf{s}_0}\left\{\Delta_{\mathbf{s}_0}^{\mathbf{s}_0} \ln p(\mathbf{s}_0)\right\}$ is derived from the prior distribution of the state [50] and where

$$\mathbf{D}_{k-1}^{11} = \mathbb{E}_{p_{0:k}}\left[-\Delta_{\mathbf{s}_{k-1}}^{\mathbf{s}_{k-1}} \ln p(\mathbf{s}_k|\mathbf{s}_{k-1})\right] = \mathbf{A}^\mathsf{T}\mathbf{Q}^{-1}\mathbf{A}, \quad (17)$$

$$\mathbf{D}_{k-1}^{12} = \mathbb{E}_{p_{0:k}}\left[-\Delta_{\mathbf{s}_{k-1}}^{\mathbf{s}_k} \ln p(\mathbf{s}_k|\mathbf{s}_{k-1})\right] = -\mathbf{A}^\mathsf{T}\mathbf{Q}^{-1}, \quad (18)$$

$$\mathbf{D}_{k-1}^{21} = \left(\mathbf{D}_{k-1}^{12}\right)^\mathsf{T}, \quad (19)$$

$$\mathbf{D}_{k-1}^{22} = \mathbb{E}_{p_{0:k}}\left[-\Delta_{\mathbf{s}_k}^{\mathbf{s}_k} \ln p(\mathbf{s}_k|\mathbf{s}_{k-1}) - \Delta_{\mathbf{s}_k}^{\mathbf{s}_k} \ln p(\mathbf{z}_k|\mathbf{s}_k)\right]$$
$$= \mathbf{Q}^{-1} + \mathbf{J}_k^\mathrm{D}, \quad (20)$$

where $\mathbf{J}_k^{\mathrm{D}}$ is the expectation of the Hessian matrix with respect to the state and measurements as [50]

$$
\begin{aligned}
\mathbf{J}_k^{\mathrm{D}} &= \mathbb{E}_{p_{0:k}}\left\{-\Delta_{\mathbf{s}_k}^{\mathbf{s}_k}\ln p\left(\mathbf{z}_k|\mathbf{s}_k\right)\right\} \\
&= \mathbb{E}_{\mathbf{s}_k|\mathbf{s}_{k-1}}\left\{\mathbb{E}_{\mathbf{z}_k|\mathbf{s}_k}\left\{-\Delta_{\mathbf{s}_k}^{\mathbf{s}_k}\ln p\left(\mathbf{z}_k|\mathbf{s}_k\right)\right\}\right\} \\
&= \mathbb{E}_{\mathbf{s}_k|\mathbf{s}_{k-1}}\left\{\tilde{\mathbf{J}}_k^{\mathrm{D}}\right\},
\end{aligned}
\tag{21}
$$

with $\tilde{\mathbf{J}}_k^{\mathrm{D}}$ being the non-Bayesian data FIM of size $N_{\mathrm{s}} \times N_{\mathrm{s}}$. Unfortunately, the expectation in (21) cannot be easily derived, but it is often approximated using Monte Carlo integration [50]. Indeed, we can separate the contribution deriving from the collected data and the prior information, thus writing

$$
\mathbf{J}_k = \mathbf{J}_{k|k-1}^{\mathrm{P}} + \mathbf{J}_k^{\mathrm{D}},
\tag{22}
$$

where $\mathbf{J}_{k|k-1}^{\mathrm{P}} = \mathbf{Q}^{-1} - \mathbf{D}_{k-1}^{21}\left(\mathbf{J}_{k-1} + \mathbf{D}_{k-1}^{11}\right)^{-1}\mathbf{D}_{k-1}^{12}$ contains the propagation information. In the sequel, we will find closed-form solutions for $\tilde{\mathbf{J}}_k^{\mathrm{D}}$ to better investigate the behaviour in near– and far–field regions. In the case study of Sec. V, we use the Bayesian FIM in (22) as a benchmark for practical tracking algorithms.

B. A Near–Field vs. Far–field Fisher Information Analysis

We now investigate the behavior of the non-Bayesian data FIM when the target approaches the Fraunhofer distance, that is, when $d_k = d_{\mathsf{F}}$, and when it is far from the radiating near–field region, i.e., $d_k \gg d_{\mathsf{F}}$ (far–field).

Proposition 1 (FIM on Source State). *Under the observation model in* (6)-(7) *and weak regularity conditions for* $p\left(\mathbf{z}_k|\mathbf{s}_k\right)$ [51], *the positioning information carried by the data FIM vanishes when the distance increases, i.e.,*

$$
\begin{aligned}
\tilde{\mathbf{J}}_k^{\mathrm{D}} &\triangleq \mathbb{E}_{\mathbf{z}_k|\mathbf{s}_k}\left\{\nabla_{\mathbf{s}_k}^{\mathsf{T}}\ln p\left(\mathbf{z}_k|\mathbf{s}_k\right)\nabla_{\mathbf{s}_k}\ln p\left(\mathbf{z}_k|\mathbf{s}_k\right)\right\} \\
&= \frac{1}{\sigma_\eta^2}\nabla_{\mathbf{s}_k}^{\mathsf{T}}h\left(\mathbf{p}_k\right)\nabla_{\mathbf{s}_k}h\left(\mathbf{p}_k\right)\underset{d_k \gg d_{\mathsf{F}}}{\longrightarrow}\mathbf{0}_{N_{\mathrm{s}}},
\end{aligned}
\tag{23}
$$

where $\mathbf{0}_{N_{\mathrm{s}}}$ *is an all-zero matrix of size* $N_{\mathrm{s}} \times N_{\mathrm{s}}$.

Proof. All the entries of the data FIM,[5] given by

$$
\left\{\tilde{\mathbf{J}}_k^{\mathrm{D}}\right\}_{i,j} = \frac{1}{\sigma_\eta^2}\left(\frac{2\pi}{\lambda}\right)^2\sum_{n=0}^{N-1}\frac{\partial\Delta d_{n,k}}{\partial[\mathbf{s}_k]_j}\cdot\frac{\partial\Delta d_{n,k}}{\partial[\mathbf{s}_k]_i}\underset{d_k \gg d_{\mathsf{F}}}{\longrightarrow}0,
\tag{24}
$$

$\forall i,j = 1,\ldots,N_{\mathrm{s}}$, tend to be zero since

$$
\frac{\partial\Delta d_{n,k}}{\partial[\mathbf{s}_k]_i}\underset{d_k \gg d_{\mathsf{F}}}{\longrightarrow}0, \qquad \forall i = 1,\ldots,N_{\mathrm{s}}.
\tag{25}
$$

as demonstrated in Appendix A. $\square$

In the next, we will show that, when moving towards the far–field region, such vanishing of information is only caused by the loss of the distance information, whereas the angles can still be inferred from the collected phases. To analyze this point, we derive the single components of the FIM on the

---

[5]In order to meet the regularity conditions, e.g., to let $\nabla_{\mathbf{s}_k}\ln p\left(\mathbf{z}_k|\mathbf{s}_k\right)$ exist and be finite, the derivatives of $h_n(\mathbf{p}_k)$ with respect to $\mathbf{s}_k$ are taken equal to the left and right derivatives in the discontinuous points, which is equivalent to substituting $h_n(\mathbf{p}_k)$ with $\Delta\vartheta_{n,k}$ in the derivatives.

distance and angle parameters, namely $\xi_k \in \{d_k, \theta_k, \phi_k\}$. We have

$$
\tilde{J}_k^{\mathrm{D}}\left(\xi_k\right) \triangleq \mathbb{E}_{\mathbf{z}_k|\xi_k}\left\{\left(\frac{\partial\ln p\left(\mathbf{z}_k|\xi_k\right)}{\partial\xi_k}\right)^2\right\} \in \mathbb{R},
\tag{26}
$$

where the gradient of the log-likelihood is given by

$$
\frac{\partial\ln p\left(\mathbf{z}_k|\xi_k\right)}{\partial\xi_k} = \frac{1}{\sigma_\eta^2}\sum_{n=0}^{N-1}\frac{\partial h_n\left(\xi_k\right)}{\partial\xi_k}\left(z_{n,k} - h_n\left(\xi_k\right)\right).
\tag{27}
$$

In the next, for notation simplicity, we omit the time index k. Moreover, we refer to $\tilde{J}_k^{\mathrm{D}}\left(\xi_k\right)$ as FIM even if it is a scalar.

Proposition 2 (FIMs on Distance and Angles). *Under the observation model in* (6)-(7) *and weak regularity conditions for* $p\left(\mathbf{z}_k|\xi_k\right)$, *the FIMs for distance and angles for both near– and far–field regions (for any value of* d*) and for any geometry (i.e., for any* d_{n0}*,* g_n*) are*

$$
\begin{aligned}
\tilde{J}^{\mathrm{D}}\left(d\right) = {} & \frac{4\pi^2}{\lambda^2\sigma_\eta^2}\sum_{n=0}^{N-1}\frac{1}{d^2 + d_{n0}^2 - 2g_n d_{n0}d}\cdot \\
&\cdot\left[2d^2 + d_{n0}^2\left(g_n^2 + 1\right) - 4g_n d d_{n0} + \right. \\
&\left. - 2(d - g_n d_{n0})\sqrt{d^2 + d_{n0}^2 - 2g_n d d_{n0}}\right],
\end{aligned}
\tag{28}
$$

$$
\tilde{J}^{\mathrm{D}}\left(\beta\right) = \frac{4\pi^2}{\lambda^2\sigma_\eta^2}\sum_{n=0}^{N-1}\frac{d^2 d_{n0}^2}{d_{n0}^2 + d^2 - 2g_n d d_{n0}}\left(\frac{\partial g_n}{\partial\beta}\right)^2,
\tag{29}
$$

where $\beta \in \{\theta, \phi\}$ *can be either the elevation or azimuth angle.*

Proof. See Appendix B. $\square$

Because the FIMs in (28)-(29) are not easy to interpret, we further simplify them by focusing on different planar array geometries, i.e., on the uniform circular array (UCA) and on URA, as well as on uniform linear array (ULA) as a specific case of URA. However, note that, for 3D localization, a planar geometry is needed to estimate the elevation angle and allows positioning.

C. UCA Configuration

We now provide assumptions, propositions and remarks when a UCA geometry is considered at the receiver side.

Assumption 1 (UCA). *The distance and azimuth angle between the* nth *antenna and the reference location are* $d_{n0} = D/2$*,* $\phi_{n0} = \frac{\pi}{2}$*,* $\forall n = 1,\ldots,(N-1)$*, whereas the elevation angle is set to* $\theta_{n0} = \frac{n2\pi}{N}$ *(lying on* YZ *plane).*

Proposition 3 (FIMs for UCA). *Under Assumption 1 of UCA, the FIMs in* (28)-(29) *for a generic source position are*

$$
\begin{aligned}
\tilde{J}^{\mathrm{D}}\left(d\right) = {} & \frac{4\pi^2}{\lambda^2\sigma_\eta^2}\sum_{n=0}^{N-1}\frac{1}{4d^2 + D^2 - 4g_n d D}\cdot \\
&\cdot\left[8d^2 + D^2\left(g_n^2 + 1\right) - 8g_n d D + \right. \\
&\left. - 2(2d - g_n D)\sqrt{4d^2 + D^2 - 4g_n d D}\right],
\end{aligned}
\tag{30}
$$

$$\tilde{J}^{\mathrm{D}}\left(\beta\right) = \frac{4\,\pi^2}{\lambda^2\,\sigma_\eta^2} \sum_{n=0}^{N-1} \frac{d^2\,D^2}{D^2 + 4\,d^2 - 4\,g_n\,d\,D} \left(\frac{\partial g_n}{\partial\beta}\right)^2, \quad (31)$$

with $\beta \in \{\theta, \phi\}$.

Proof. From (28)-(29), they are obtained by substituting $(d_{n0}, \phi_{n0}, \theta_{n0})$ with the values in Assumption 1. $\qquad\square$

Remark 1 (Asymptotic Analysis for UCA). From the FIMs in (30)-(31) valid for a UCA and without any assumption of the source position, we obtain the FIMs at the boundary of the Fresnel region (i.e., for $d_k = d_{\mathrm{F}}$) that are

$$\tilde{J}^{\mathrm{D}}\left(d\right) = \frac{4\,\pi^2}{\lambda^2\,\sigma_\eta^2} \sum_{n=0}^{N-1} \frac{1}{1 + \frac{\lambda^2}{16\,D^2} - g_n\frac{\lambda}{2\,D}} \cdot$$
$$\cdot \left[2 + \frac{\lambda^2}{16\,D^2}\left(g_n^2 + 1\right) - \frac{g_n\,\lambda}{D} + \right.$$
$$\left. - \left(2 - g_n\frac{\lambda}{2D}\right)\sqrt{1 + \frac{\lambda^2}{16\,D^2} - g_n\frac{\lambda}{2\,D}}\right], \quad (32)$$

$$\tilde{J}^{\mathrm{D}}\left(\beta\right) = \frac{\pi^2\,D^2}{\lambda^2\,\sigma_\eta^2} \sum_{n=0}^{N-1} \frac{1}{1 + \frac{\lambda^2}{16\,D^2} - g_n\frac{\lambda}{2\,D}} \left(\frac{\partial g_n}{\partial\beta}\right)^2, \quad (33)$$

with $\beta \in \{\theta, \phi\}$, and the FIMs for $d \gg d_{\mathrm{F}}$ that are

$$\tilde{J}^{\mathrm{D}}\left(d\right) = 0, \quad (34)$$

$$\tilde{J}^{\mathrm{D}}\left(\beta\right) = \frac{\pi^2\,D^2}{\lambda^2\,\sigma_\eta^2} \sum_{n=0}^{N-1} \left(\frac{\partial g_n}{\partial\beta}\right)^2. \quad (35)$$

Note that the expressions in (32)-(33) coincide with those in (34)-(35) when $\lambda \ll D$, e.g., when mm-waves are considered.

Now to further simplify the expressions, we constrain the source position along the central perpendicular line (CPL) as in [37].

Assumption 2 (Source Position). *The source is on the central perpendicular line, along the X-axis, so that $\theta = \frac{\pi}{2}, \phi = 0$, such that $g_n = 0, \forall\, n = 0, \ldots, N-1$.*

Proposition 4 (FIMs for UCA and Source on CPL). *Under Assumptions 1 and 2, the FIMs in (28)-(29) for a UCA on the YZ-plane and a target on the X-axis are*

$$\tilde{J}^{\mathrm{D}}\left(d\right) = \frac{4\,N\,\pi^2}{\lambda^2\,\sigma_\eta^2} \cdot \frac{2 + \frac{D^2}{4\,d^2} - 2\sqrt{1 + \frac{D^2}{4\,d^2}}}{1 + \frac{D^2}{4\,d^2}}, \quad (36)$$

$$\tilde{J}^{\mathrm{D}}\left(\theta\right) = \tilde{J}^{\mathrm{D}}\left(\phi\right) = \frac{N\,\pi^2}{2\,\lambda^2\sigma_\eta^2} \frac{D^2}{1 + \frac{D^2}{4\,d^2}}. \quad (37)$$

Proof. See Appendix C. $\qquad\square$

Remark 2 (Asymptotic Analysis for UCA and Source on CPL). From (36)-(37), we obtain the FIMs at the boundary of the Fresnel region ($d_k = d_{\mathrm{F}}$),

$$\tilde{J}^{\mathrm{D}}\left(d\right) = \frac{4\,N\,\pi^2}{\lambda^2\,\sigma_\eta^2} \frac{2 + \frac{\lambda^2}{16\,D^2} - 2\sqrt{1 + \frac{\lambda^2}{16\,D^2}}}{1 + \frac{\lambda^2}{16\,D^2}}, \quad (38)$$

$$\tilde{J}^{\mathrm{D}}\left(\theta\right) = \tilde{J}^{\mathrm{D}}\left(\phi\right) = \frac{N\,\pi^2}{2\,\lambda^2\sigma_\eta^2} \frac{D^2}{1 + \frac{\lambda^2}{16\,D^2}}, \quad (39)$$

and, for $d_k \gg d_{\mathrm{F}}$ (far–field region), we get

$$\tilde{J}^{\mathrm{D}}\left(d\right) = 0, \quad (40)$$

$$\tilde{J}^{\mathrm{D}}\left(\theta\right) = \tilde{J}^{\mathrm{D}}\left(\phi\right) = \frac{D^2\,N\,\pi^2}{2\,\lambda^2\sigma_\eta^2}. \quad (41)$$

The results show the dependence of the FIMs on the diameter D of the array and the number of measurements N. Further, they also reveal that the FIMs are inversely proportional to the measurement noise variance σ_η^2 and squared wavelength λ^2.

Note that $\tilde{J}^{\mathrm{D}}\left(\theta\right)$ and $\tilde{J}^{\mathrm{D}}\left(\phi\right)$ in (39) tend to their asymptotic values in (41) because $\frac{\lambda^2}{16\,D^2} \ll 1$. Consequently, the performance is constant within the Fresnel region. According to this result, outside the near–field region bounded by d_{F}, it is not possible to retrieve the target position because the CoA tends to vanish, despite the feasibility of estimating the angles.

D. URA and ULA Configurations

We now provide assumptions, propositions and remarks when a URA geometry is considered at the receiver, and we draw the ULA as a specific case of URA.

We consider a URA lying on the YZ-plane with $\mathbf{q}_0 = [0, 0, 0]$ and antennas equally spaced by $\lambda/2$. The generic nth antenna is located at $\mathbf{q}_n = \frac{\lambda}{2}\,[0, n_{\mathrm{y}}, n_{\mathrm{z}}]$ with $n_{\mathrm{y}} = \lfloor\frac{n}{N_{\mathrm{z}}}\rfloor$ and $n_{\mathrm{z}} = (n \bmod N_{\mathrm{z}})$ being the antenna index along the Y- and Z-axis, respectively. Moreover, it can be noted that a ULA lying along the Y-axis is a special case of URA with $N_{\mathrm{z}} = 0$, i.e., $\mathbf{q}_n = \frac{\lambda}{2}\,[0, n, 0]$, with $n = 0, \ldots, (N-1)$. We, thus, have the following two assumptions

Assumption 3 (URA). *The distance, azimuth and elevation angles between the nth antenna and the reference location are $d_{n0} = \frac{\lambda}{2}\sqrt{n_{\mathrm{y}}^2 + n_{\mathrm{z}}^2} \triangleq \frac{\lambda}{2}\,\tilde{n}$, $\phi_{n0} = \frac{\pi}{2}$, $\forall n$, and $\theta_{n0} = \mathrm{acos}\left(\frac{n_{\mathrm{z}}}{\tilde{n}}\right) \in \left[0, \frac{\pi}{2}\right]$, respectively.*

Assumption 4 (ULA). *The distance, azimuth and elevation angles between the nth antenna and the reference location are $d_{n0} = \frac{\lambda}{2}\,n$, $\phi_{n0} = \frac{\pi}{2}$, and $\theta_{n0} = \frac{\pi}{2}$ $\forall n = 0, \ldots, (N-1)$, respectively. In this case, we have $g_n = \sin(\theta)\,\sin(\phi)$, $\forall n$.*

Following the same principle as for the UCA, starting from (28)-(29), we can derive the FIMs for distance and angles valid for the URA and ULA.

Proposition 5 (FIMs for URA and ULA). *Under Assumptions 3 and 4, considering a URA on the YZ-plane, the FIMs in (28)-(29) become*

$$\tilde{J}^{\mathrm{D}}\left(d\right) = \frac{8\,\pi^2}{\lambda^2\,\sigma_\eta^2} \sum_{n=0}^{N-1} \frac{1}{4\,d^2 + \lambda^2\,\tilde{n}^2 - 4\,g_n\,\lambda\,\tilde{n}\,d} \cdot$$
$$\cdot \left[4\,d^2 + \frac{\lambda^2}{2}\,\tilde{n}^2\left(g_n^2 + 1\right) - 4\,g_n\,d\,\lambda\,\tilde{n} + \right.$$
$$\left. - \left(2\,d - g_n\lambda\,\tilde{n}\right)\sqrt{4\,d^2 + \lambda^2\,\tilde{n}^2 - 4\,g_n d\,\lambda\,\tilde{n}}\right], \quad (42)$$

$$\tilde{J}^{\mathrm{D}}\left(\beta\right) = \frac{4\,\pi^2}{\sigma_\eta^2} \sum_{n=0}^{N-1} \frac{d^2\,\tilde{n}^2}{4\,d^2 + \lambda^2\,\tilde{n}^2 - 4\,g_n\,d\,\lambda\,\tilde{n}} \left(\frac{\partial g_n}{\partial\beta}\right)^2, \quad (43)$$

with $\beta \in \{\theta, \phi\}$. *The FIMs for ULA can be obtained by replacing $\tilde{n}$ with n.*
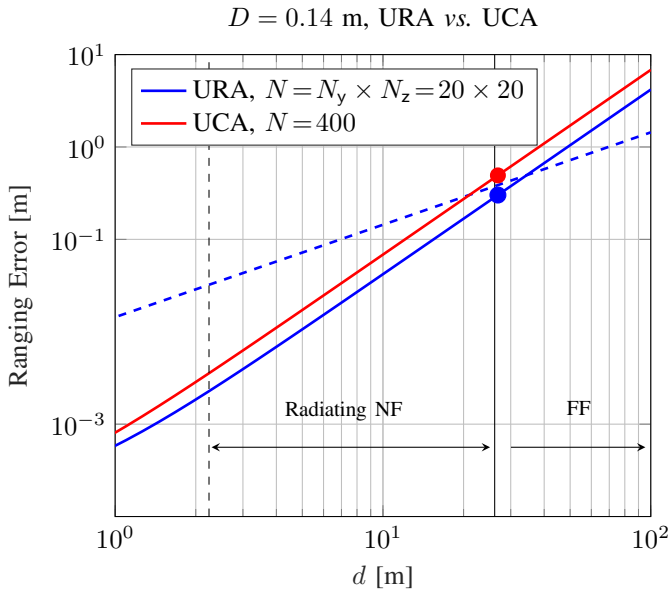
Fig. 3. Ranging error $\sqrt{\left[\tilde{J}^{\mathrm{D}}\left(d\right)\right]^{-1}}$ as a function of the source distance d. We set $f_p = 28\,\mathrm{GHz}$ and $\sigma_\eta = 20°$, NF and FF stand for near–field and far–field, respectively. We considered an URA and UCA geometry for a fixed $D = 0.14\,\mathrm{m}$. The threshold, indicated with a dashed line, corresponds to ranging error of $1/10$ of the actual distance.
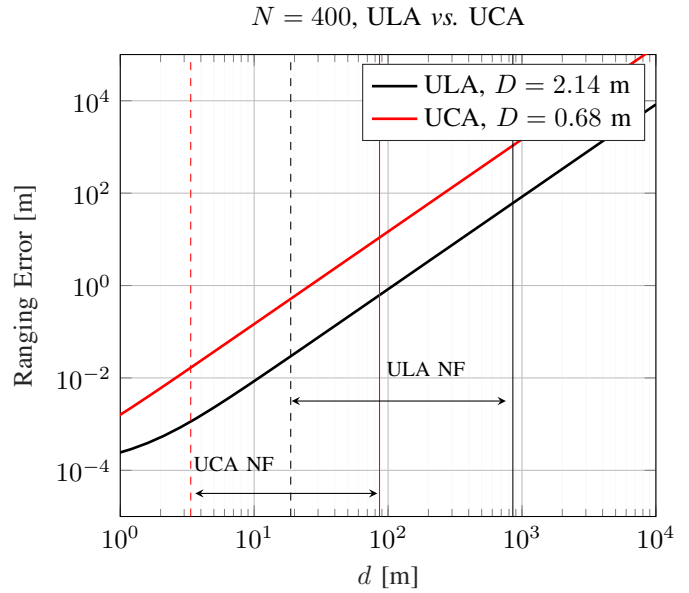

Fig. 4. Ranging error $\sqrt{\left[\tilde{J}^{\mathrm{D}}\left(d\right)\right]^{-1}}$ as a function of the source distance d. We set $f_p = 28\,\mathrm{GHz}$ and $\sigma_\eta = 20°$, NF and FF stand for near–field and far–field, respectively. We considered an ULA and UCA geometry for $N = 400$ and antenna spacing of $\lambda/2$.

Remark 3 (Asymptotic Analysis for URA and ULA). From the FIMs in (42)-(43) valid for URA and ULA and without any assumption on the source position, we obtain the FIMs at the boundary of the Fresnel region that are

$$\tilde{J}^{\mathrm{D}}\left(d\right) = \frac{8\,\pi^2}{\lambda^2\,\sigma_\eta^2}\sum_{n=0}^{N-1}\frac{1}{1+\left(\frac{\tilde{n}}{\tilde{N}^2}\right)^2-2\,g_n\,\frac{\tilde{n}}{\tilde{N}^2}}\cdot$$
$$\cdot\left[1+\frac{\tilde{n}}{2\,\tilde{N}^2}\left(\frac{\tilde{n}}{\tilde{N}^2}(g_n^2+1)-4\,g_n\right)+\right.$$
$$\left.-\left(1-2\,g_n\frac{\tilde{n}}{\tilde{N}^2}\right)\sqrt{1+\left(\frac{\tilde{n}}{\tilde{N}^2}\right)^2-2\,g_n\,\frac{\tilde{n}}{\tilde{N}^2}}\right], \quad (44)$$

$$\tilde{J}^{\mathrm{D}}\left(\beta\right) = \frac{\pi^2}{\sigma_\eta^2}\sum_{n=0}^{N-1}\frac{\tilde{n}^2}{1+\left(\frac{\tilde{n}}{\tilde{N}^2}\right)^2-2\,g_n\,\frac{\tilde{n}}{\tilde{N}^2}}\left(\frac{\partial g_n}{\partial\beta}\right)^2, \quad (45)$$

with $\beta \in \{\theta, \phi\}$, $D = \frac{\lambda}{2}\tilde{N} \triangleq \frac{\lambda}{2}\sqrt{N_y^2+N_z^2}$, and the FIMs for $d \gg d_\mathrm{F}$ that are

$$\tilde{J}^{\mathrm{D}}\left(d\right) = 0, \quad (46)$$

$$\tilde{J}^{\mathrm{D}}\left(\beta\right) = \frac{\pi^2}{\sigma_\eta^2}\sum_{n=0}^{N-1}\tilde{n}^2\left(\frac{\partial g_n}{\partial\beta}\right)^2. \quad (47)$$

These same expressions hold for ULA by replacing $\tilde{n}$ with n.

Proposition 6 (FIMs for URA and Source on CPL). *Under Assumptions 2 and 3, considering a URA on the YZ-plane*

and a source on the X-axis, the FIMs in (28)-(29) *become*

$$\tilde{J}^{\mathrm{D}}\left(d\right) = \frac{4\,\pi^2}{\lambda^2\,\sigma_\eta^2}\sum_{n=0}^{N-1}\frac{8\,d^2+\lambda^2\,\tilde{n}^2-4\,d\,\sqrt{4\,d^2+\lambda^2\,\tilde{n}^2}}{4\,d^2+\lambda^2\,\tilde{n}^2},$$
$$(48)$$

$$\tilde{J}^{\mathrm{D}}\left(\theta\right) = \frac{4\,\pi^2}{\sigma_\eta^2}\sum_{n=0}^{N-1}\frac{n_z^2\,d^2}{\tilde{n}^2\,\lambda^2+4\,d^2}, \quad (49)$$

$$\tilde{J}^{\mathrm{D}}\left(\phi\right) = \frac{4\,\pi^2}{\sigma_\eta^2}\sum_{n=0}^{N-1}\frac{n_y^2\,d^2}{\tilde{n}^2\,\lambda^2+4\,d^2}. \quad (50)$$

Proof. From (28)-(29), the FIMs are obtained by substituting $(d_{n0}, \phi_{n0}, \theta_{n0})$ according to Assumption 2 and (θ, ϕ) according to Assumption 3. $\quad\square$

Proposition 7 (FIMs for ULA and Source on CPL). *Under Assumptions 2 and 4, considering a ULA along the y-axis and a source on the X-axis, the FIMs in* (28)-(29) *become*

$$\tilde{J}^{\mathrm{D}}\left(d\right) = \frac{4\,\pi^2}{\lambda^2\,\sigma_\eta^2}\sum_{n=0}^{N-1}\frac{8\,d^2+\lambda^2\,n^2-4\,d\sqrt{4\,d^2+\lambda^2\,n^2}}{4\,d^2+\lambda^2\,n^2},$$
$$(51)$$

$$\tilde{J}^{\mathrm{D}}\left(\theta\right) = 0, \quad (52)$$

$$\tilde{J}^{\mathrm{D}}\left(\phi\right) = \frac{4\,\pi^2\,d^2}{\sigma_\eta^2}\sum_{n=0}^{N-1}\frac{n^2}{4\,d^2+\lambda^2\,n^2}. \quad (53)$$

It is worth noticing that the estimation of the elevation angle is not feasible given the considered linear array geometry.

Algorithm 1: Extended Kalman Filter

Initialization for $k = 1$:

Initialize the state $\mathbf{s}_0 \sim \mathcal{N}\left(\mathbf{s}_0; \mathbf{m}_0, \mathbf{P}_0\right)$;

for $k = 1, \ldots, K$ **do**

  Measurement update;

  Calculate the innovation and its covariance;

  $\mathbf{v}_k = \mathbf{z}_k - h\left(\mathbf{m}_{k|k-1}\right);$ *size:* $(N \times 1)$

  $\mathbf{S}_k = \mathbf{H}_k \mathbf{P}_{k|k-1} \mathbf{H}_k^\mathsf{T} + \mathbf{R}_k;$ $(N \times N)$

  Compute the Kalman gain;

  $\mathbf{K}_k = \mathbf{P}_{k|k-1} \mathbf{H}_k^\mathsf{T} \mathbf{S}_k^{-1};$ $(N_\mathsf{s} \times N)$

  Update the posterior state estimate and covariance;

  $\mathbf{m}_{k|k} = \mathbf{m}_{k|k-1} + \mathbf{K}_k \mathbf{v}_k;$ $(N_\mathsf{s} \times 1)$

  $\mathbf{P}_{k|k} = \mathbf{P}_{k|k-1} - \mathbf{K}_k \mathbf{S}_k \mathbf{K}_k^\mathsf{T};$ $(N_\mathsf{s} \times N_\mathsf{s})$

  State Estimation;

  Estimate the state;

  $\hat{\mathbf{s}}_k = \mathbf{m}_{k|k};$ $(N_\mathsf{s} \times 1)$

  Time Update;

  Predict the prior state estimate and covariance;

  $\mathbf{m}_{k+1|k} = \mathbf{A}\, \mathbf{m}_{k|k};$ $(N_\mathsf{s} \times 1)$

  $\mathbf{P}_{k+1|k} = \mathbf{A}\, \mathbf{P}_{k|k}\, \mathbf{A}^\mathsf{T} + \mathbf{Q};$ $(N_\mathsf{s} \times N_\mathsf{s})$

end

Algorithm 2: Particle Filter

Initialization for $k = 1$:

Initialize the particles $\mathbf{s}_{m,1} \sim p_0$ and their weights $w_{m,1|0} = 1/M, \; \forall m$;

for $k = 1, \ldots, K$ **do**

  Measurement update;

  Update the weights according to the likelihood;

  $w_{m,k} \triangleq w_{m,k|k} = w_{m,k|k-1}\, p\left(\mathbf{z}_k | \mathbf{s}_{m,k}\right);$

  Normalize the weights;

  $w_{m,k|k} = w_{m,k|k} / \sum_m^M w_{m,k|k};$

  State Estimation;

  Estimate the state;;

  $\hat{\mathbf{s}}_k = \sum_m^M w_{m,k|k}\, \mathbf{s}_{m,k};$

  Resampling;

  Resample using multinomial resampling;

  Time Update;

  Predict particles and weights according to the proposal in (62);

  $\mathbf{s}_{m,k+1} \sim \pi\left(\mathbf{s}_{k+1} | \mathbf{s}_{m,k}, \mathbf{z}_{k+1}\right)$

  $w_{m,k+1|k} = w_{m,k|k}\, \dfrac{p(\mathbf{s}_{m,k+1} | \mathbf{s}_{m,k})}{\pi(\mathbf{s}_{m,k+1} | \mathbf{s}_{m,k}, \mathbf{z}_{k+1})};$

end

Remark 4 (Asymptotic Analysis for URA-ULA and source on CPL). For asymptotic considerations, we specialize (48)-(50) at the boundary of the Fresnel region ($d = d_\mathrm{F}$), thus yielding

$$\tilde{J}^\mathrm{D}(d) = \frac{4\,\pi^2}{\lambda^2\, \sigma_\eta^2} \sum_{n_\mathsf{y},n_\mathsf{z}} \frac{2 + \left(\frac{\tilde{n}}{N^2}\right)^2 - 2\sqrt{1 + \left(\frac{\tilde{n}}{N^2}\right)^2}}{1 + \left(\frac{\tilde{n}}{N^2}\right)^2}, \quad (54)$$

$$\tilde{J}^\mathrm{D}(\theta) = \frac{\pi^2}{\sigma_\eta^2} \sum_{n_\mathsf{y},n_\mathsf{z}} \frac{n_\mathsf{z}^2}{1 + \left(\frac{\tilde{n}}{N^2}\right)^2}, \quad (55)$$

$$\tilde{J}^\mathrm{D}(\theta) = \frac{\pi^2}{\sigma_\eta^2} \sum_{n_\mathsf{y},n_\mathsf{z}} \frac{n_\mathsf{y}^2}{1 + \left(\frac{\tilde{n}}{N^2}\right)^2}, \quad (56)$$

where $\sum_{n_\mathsf{y},n_\mathsf{z}} = \sum_{n_\mathsf{y}=0}^{N_\mathsf{y}-1} \sum_{n_\mathsf{z}=0}^{N_\mathsf{z}-1}$, whereas, for $d_k \gg d_\mathrm{F}$, we obtain

$$\tilde{J}^\mathrm{D}(d) = 0, \quad (57)$$

$$\tilde{J}^\mathrm{D}(\theta) = \frac{\pi^2}{\sigma_\eta^2} \frac{N_\mathsf{y}\, N_\mathsf{z}\, (2\, N_\mathsf{z} - 1)\, (N_\mathsf{z} - 1)}{6}, \quad (58)$$

$$\tilde{J}^\mathrm{D}(\phi) = \frac{\pi^2}{\sigma_\eta^2} \frac{N_\mathsf{y}\, N_\mathsf{z}\, (2N_\mathsf{y} - 1)\, (N_\mathsf{y} - 1)}{6}. \quad (59)$$

The asymptotic FIMs for ULA are obtained by replacing in (57)-(59), the parameters $\left\{n_\mathsf{y}, n_\mathsf{z}, \tilde{n}, \tilde{N}, N_\mathsf{y}, N_\mathsf{z}\right\}$ with $\{n, 0, n, N, N, 0\}$.

Notably, due to the considered system geometry, the number of antennas on the Z-axis, i.e., N_z, augments the information in estimating the elevation angle, whereas N_y plays the same role for the azimuth.

E. Numerical Results

We now provide some results according to the aforementioned considerations. Figs. 3-4 display the square root of the inverse of the ranging FIM $\tilde{J}^\mathrm{D}(d)$ as a function of the source-array distance. More specifically, Fig. 3 is obtained by fixing the array aperture (i.e., D) and the number of antennas (i.e., N), and by varying the array geometries (i.e., URA *vs* UCA) and the antenna spacing; Fig. 4 results from a fixed number of antennas (i.e., N) and spacing (i.e., $d_\mathsf{ant} = \lambda/2$), while varying the array aperture and geometries (i.e., ULA *vs* UCA).

We observe from the obtained results that the ranging information depends on the ratio d/D, and tends to decrease when this ratio becomes larger. Fig. 3 also shows a threshold line that corresponds to an error of 0.1% of the actual distance. We can see that the inverse of the ranging FIM is above the threshold outside the Fraunhofer boundary. Moreover, it is worth noticing that the ranging performance does not depend on the geometry provided that D is the same.

Since the tracking performance is mainly driven by the array size D, in the case study of Sec. V-A, we only focus on URA array configuration.

IV. TRACKING ALGORITHMS

We now provide an overview of some well-known tracking algorithms to assess their performance and their robustness, using the state-space model in (3)-(4), with non–linear Gaussian observation model and considering the CoA for positioning.

A. Extended Kalman Filter

Among the Bayesian estimators, we start by describing the EKF accounting for the CoA information in (4). The state is described by a Gaussian distribution, i.e., $\mathbf{s}_k \sim \mathcal{N}\left(\mathbf{s}_k; \mathbf{m}_k, \mathbf{P}_k\right)$, with $\mathbf{m}_k \in \mathbb{R}^{N_\mathsf{s}}$ and $\mathbf{P}_k \in \mathbb{R}^{N_\mathsf{s}^2}$ being the posterior mean vector and covariance matrix of the state, $\forall k = 0, \ldots, K$. The major steps are reported in Algorithm 1, and are as follows [45]

Initialization: The EKF is initialized by a prior distribution of the state, i.e., $\mathbf{s}_0 \sim p_0 = \mathcal{N}\left(\mathbf{s}_0; \mathbf{m}_0, \mathbf{P}_0\right)$.

Measurement update: The EKF requires the evaluation of the Jacobian matrix associated to the linearization of the observation model $h\left(\mathbf{p}_k\right)$ [45], that can be written as

$$\mathbf{H}_k \triangleq \nabla_{\mathbf{s}_k} h\left(\mathbf{p}_k\right), \tag{60}$$

of size $N \times N_{\mathrm{s}}$, where $\nabla_{\mathbf{s}_k}$ is the gradient with respect to the state vector and where the nth row of $\mathbf{H}_k$ is given by

$$\{\mathbf{H}_k\}_n = \nabla_{\mathbf{s}_k} h_n\left(\mathbf{p}_k\right) = \frac{2\pi}{\lambda} \nabla_{\mathbf{s}_k} \Delta d_{n,k}\left(\mathbf{p}_k\right), \tag{61}$$

with $n = 0, \dots, N-1$ and where $\{\cdot\}_n$ picks the nth row of $\mathbf{H}_k$ (refer to Appendix A). The Jacobian is evaluated at $\mathbf{s}_k = \mathbf{m}_{k|k-1}$ where $\mathbf{m}_{k|k-1}$ is the predicted state (for $k=1$, it is $\mathbf{m}_{k|k-1} = \mathbf{m}_0$). Then, following Alg. 1, the innovation mean and covariance ($\mathbf{v}_k \in \mathbb{R}^N$, $\mathbf{S}_k \in \mathbb{R}^{N^2}$) and the Kalman gain $\mathbf{K}_k$ of size $N_{\mathrm{s}} \times N$ are computed and used to update the posterior mean vector $\mathbf{m}_{k|k}$ and covariance matrix $\mathbf{P}_{k|k}$ [45].

Time update: The EKF prediction step makes use of the transition model in (3), leading to the estimation of the expected conditional mean $\mathbf{m}_{k|k-1}$ and covariance matrix $\mathbf{P}_{k|k-1}$ for the next time instant.

B. Particle Filter

A particle filter (PF) exploits the representation of an arbitrary probability distribution function (PDF) by a set of particles and associated weights and where the sequential sampling-importance-resampling (SIR) procedure plays a central role. This approach is especially useful for nonlinear non-Gaussian models [52], [53]. The goal is the sequential estimation of a filtering distribution, i.e., $p\left(\mathbf{s}_k|\mathbf{z}_{1:k}\right)$. Indeed, this distribution cannot be analytically solved apart from very few cases and, thus, the common procedure is to exploit discrete random measures composed of particles and weights $\{\mathbf{s}_{m,k}, w_{m,k}\}_{m=1}^{M}$, that are possible values of the unknown state $\mathbf{s}_k$, where M is the number of particles [54]. Then, the PF can be described by following three major steps reported in Algorithm 2.

Sampling step: The first step is the generation of new particles at the time instant k. The particles are drawn from an importance sampling (IS) density $\pi\left(\cdot\right)$ as $\mathbf{s}_{m,k} \sim \pi\left(\mathbf{s}_k|\mathbf{s}_{m,k-1}, \mathbf{z}_{1:k}\right)$. Possible choices for the IS density are reviewed in Sec. IV-C.

Importance step: Subsequently, the weights $w_{m,k}$ associated with each particle are computed and normalized. The estimate of the state $\hat{\mathbf{s}}_k$ is inferred as a weighted sum of particles.

Resampling: Finally, to avoid the *degeneracy* problem [54] where few particles are dominant, a *resampling* strategy is typically adopted. Resampling permits particles with large weights to dominate over particles with small weights, so that at the next time instant, new particles will be generated in the region where large weights are present. After the resampling, weights are also set to be equiprobable, i.e., to $1/M$.

PFs have become a popular approach because of their ability to operate with models of any nonlinearity and with any noise distributions for as long as the likelihoods and the transition pdf that arise from the model (3)–(4) are computable.

However, their computational complexity may be high if the number of particles becomes very large [54], [55].

C. The importance sampling (IS) density

The choice of the proposal distribution is one of the most crucial and critical tasks when implementing PFs. We now describe some options that perform differently according to the quality of the adopted models.

a) IS from the prior: In this case, the IS density is set equal to the transition distribution function, which is

$$\mathbf{s}_{m,k} \sim p\left(\mathbf{s}_{m,k}|\mathbf{s}_{m,k-1}\right) = \mathcal{N}\left(\mathbf{s}_{m,k}; \mathbf{A}\,\mathbf{s}_{m,k-1}, \mathbf{Q}\right), \tag{62}$$

of size $N_{\mathrm{s}} \times 1$, with $m = 1, \dots, M$, and with $\mathbf{s}_{m,0} \sim p_0 = p\left(\mathbf{s}_0\right)$ being the prior information on the state. As a result, the weights of the particles can be computed using the likelihood function (LF) of each particle, i.e.,

$$w_{m,k} = w_{m,k-1}\, p\left(\mathbf{z}_k|\mathbf{s}_{m,k}\right). \tag{63}$$

A major drawback of this solution is that particles are propagated without taking into consideration the newest measurements $\mathbf{z}_k$. Even though the latest measurement is not used for generating new particles, PFs work surprisingly well in most settings. One exception is when the likelihood of the particles is very sharp in comparison to the prior.

b) IS from the likelihood: In situations where the likelihood function is much more informative than the prior distribution, a possible alternative to prior IS is sampling from the likelihood. A possibility is to run a maximum likelihood estimator (MLE) at each time instant k, that, differently from Bayesian approaches, accounts only for the observation model and the latest set of measurements, while neglecting any statistical information regarding the state transition. Then, the state is inferred by solving the following maximization problem:

$$\hat{\mathbf{s}}_{\mathrm{ML},k} = \arg\max_{\mathbf{s}_k} \ln p\left(\mathbf{z}_k|\mathbf{s}_k\right), \tag{64}$$

where, since the measurements are considered independent at each antenna, we have

$$\begin{aligned} p\left(\mathbf{z}_k|\mathbf{s}_k\right) &= \prod_{n=0}^{N-1} p\left(z_{n,k}|\mathbf{s}_k\right) = \prod_{n=0}^{N-1} \mathcal{N}\left(z_{n,k}; h_n\left(\mathbf{p}_k\right), \sigma_\eta^2\right) \\ &= \frac{1}{\sqrt{2\pi}\,\sigma_\eta} \exp\left(-\frac{\sum_{n=0}^{N-1}\left(z_{n,k}-h_n\left(\mathbf{p}_k\right)\right)^2}{2\,\sigma_\eta^2}\right). \end{aligned} \tag{65}$$

Then, the particles are generated from a Gaussian distribution centered at the maximum likelihood (ML) estimate by

$$\mathbf{s}_{m,k} \sim \mathcal{N}\left(\mathbf{s}_{m,k}; \hat{\mathbf{s}}_{\mathrm{ML},k}, \mathbf{P}_{\mathrm{ML},k}\right), \tag{66}$$

where $\mathbf{P}_{\mathrm{ML},k}$ is the covariance matrix of size $N_{\mathrm{s}} \times N_{\mathrm{s}}$ that determines how the particles are spread around the ML estimate. With such choice of IS, the weights are updated by

$$w_{m,k} = w_{m,k-1}\frac{p\left(\mathbf{z}_k|\mathbf{s}_{m,k}\right) p\left(\mathbf{s}_{m,k}|\mathbf{s}_{m,k-1}\right)}{\mathcal{N}\left(\mathbf{s}_{m,k}; \hat{\mathbf{s}}_{\mathrm{ML},k}, \mathbf{P}_{\mathrm{ML},k}\right)}. \tag{67}$$

Notably, in the considered approach it might happen that $w_{m,k} \approx 0$, $\forall\, m$, due to the mismatch between the likelihood

$p\left(\mathbf{z}_k|\mathbf{s}_{m,k}\right)$ and the transition $p\left(\mathbf{s}_{m,k}|\mathbf{s}_{m,k-1}\right)$ in (67). To overcome such an issue, we included a control such that, if all the weights are zeros (or below a certain threshold related to the numerical accuracy), we reset them to $w_{m,k} = 1/M, \forall m$.

c) Optimal IS: The use of the transition density as an importance function may create ambiguity problems because it does not depend on the new measurements $\mathbf{z}_k$. At the same time, the likelihood IS does not account for the transition model. Consequently, a possible choice for the optimal IS is to directly sample from the posterior [55]–[57]

$$\pi\left(\mathbf{s}_k|\mathbf{s}_{m,k-1},\mathbf{z}_k\right) = \frac{p\left(\mathbf{z}_k|\mathbf{s}_k\right)p\left(\mathbf{s}_k|\mathbf{s}_{m,k-1}\right)}{\int p\left(\mathbf{z}_k|\mathbf{s}_k\right)p\left(\mathbf{s}_k|\mathbf{s}_{m,k-1}\right)d\mathbf{s}_k}, \quad (68)$$

where an analytical form can be found if the observation function is linear and the noises in the state and observation equations are Gaussians and additive.

d) Local linearisation of the optimal IS: In our case, since the observation function is nonlinear, we perform a local linearisation around the predicted state, as done for the EKF, with the purpose of deriving a closed-form expression for the proposal density. In particular, we have

$$\mathbf{z}_k \approx h\left(\mathbf{s}_k^-\right) + \mathbf{H}_{k|k-1}\left(\mathbf{s}_k - \mathbf{s}_k^-\right) + \boldsymbol{\eta}_k, \quad (69)$$

where $\mathbf{s}_k^- = \mathbf{A}\,\mathbf{s}_{k-1}$ is the predicted state, $\mathbf{H}_{k|k-1} \triangleq \mathbf{H}_k\big|_{\mathbf{s}_k=\mathbf{s}_k^-}$ is the $N \times N_{\mathrm{s}}$ Jacobian matrix in (60) evaluated at the predicted state. Then, we can express (69) as a function of the state, i.e.,

$$\begin{aligned} \mathbf{s}_k &= \mathbf{H}_{k|k-1}^{\dagger}\left(\mathbf{z}_k - h\left(\mathbf{s}_k^-\right) - \boldsymbol{\eta}_k\right) + \mathbf{s}_k^- \\ &= \mathbf{H}_{k|k-1}^{\dagger}\left(\mathbf{z}_k - h\left(\mathbf{s}_k^-\right)\right) + \mathbf{s}_k^- + \tilde{\boldsymbol{\eta}}_k, \end{aligned} \quad (70)$$

where $\dagger$ is the pseudo-inverse operator, $\mathbf{H}_{k|k-1}^{\dagger}$ is the $N_{\mathrm{s}} \times N$ Moore-Penrose inverse of the predicted Jacobian matrix, $\tilde{\boldsymbol{\eta}}_k \sim \mathcal{N}\left(\tilde{\boldsymbol{\eta}}_k;\mathbf{0},\tilde{\mathbf{R}}_k\right) \in \mathbb{R}^N$ and $\tilde{\mathbf{R}}_k = \mathbf{H}_{k|k-1}^{\dagger}\mathbf{R}_k\left(\mathbf{H}_{k|k-1}^{\dagger}\right)^{\mathsf{T}} \in \mathbb{R}^{N^2}$. Consequently, by considering the product of (3)-(70) that are Gaussian densities, it is possible to derive

$$\mathbf{s}_{m,k} \sim p\left(\mathbf{s}_{m,k}|\mathbf{s}_{m,k-1},\mathbf{z}_k\right) \approx \mathcal{N}\left(\mathbf{s}_{m,k};\mathbf{m}_{m,k},\mathbf{P}_{m,k}\right), \quad (71)$$

where the mean and covariance matrix of the particle state are derived as [57]

$$\mathbf{P}_{m,k}^{-1} = \mathbf{Q}^{-1} + \tilde{\mathbf{R}}_{m,k}^{-1}, \quad (72)$$

$$\mathbf{m}_{m,k} = \mathbf{P}_{m,k}\left[\mathbf{Q}^{-1}\mathbf{s}_{m,k}^- + \mathbf{H}_{m,k|k-1}^{\mathsf{T}}\mathbf{R}^{-1}\cdot\right.$$

$$\left.\cdot\left(\mathbf{z}_k - h\left(\mathbf{s}_{m,k}^-\right) + \mathbf{H}_{m,k|k-1}\mathbf{s}_{m,k}^-\right)\right], \quad (73)$$

where $\mathbf{s}_{m,k}^- = \mathbf{A}\,\mathbf{s}_{m,k-1}$ is the predicted state for the mth particle, $\mathbf{H}_{m,k|k-1}$ and $\tilde{\mathbf{R}}_{m,k}$ are computed at the particle predicted states. In this case, the weights associated with each particle are obtained by

$$w_{m,k} = w_{m,k-1}\frac{p\left(\mathbf{z}_k|\mathbf{s}_{m,k}\right)p\left(\mathbf{s}_{m,k}|\mathbf{s}_{m,k-1}\right)}{\mathcal{N}\left(\mathbf{s}_{m,k};\mathbf{m}_{m,k},\mathbf{P}_{m,k}\right)}. \quad (74)$$

The optimal IS represents a trade-off between the prior and the likelihood IS, and it provides good performance when

both models are accurate. In the following, we evaluate and compare the performance of the described approaches.

V. CASE STUDY

A. Simulation Parameters

We now evaluate the tracking performance and the theoretical bound by varying the array size, the tracking algorithms, and the model assumptions. To this purpose, we set $\lambda = 0.01\,\mathrm{m}$, and the number of particles to $M = 1000$, if not otherwise indicated.

A large antenna array was placed in the origin, i.e., the reference location was $\mathbf{q}_0 \triangleq [x_0, y_0, z_0]^{\mathsf{T}}$ (m) $= (0, 0, 1)$, and we alternatively considered a URA lying on the YZ-plane with $N = 20 \times 20$, if not otherwise indicated.

The initial state of the target at time instant 0 was $\mathbf{s}_0 \triangleq [x_0, y_0, z_0, v_{\mathrm{x},0}, v_{\mathrm{y},0}, v_{\mathrm{z},0}]^{\mathsf{T}} = (2.5, -9.1, 1.5, 0.01, 0.97, 0)$, where the simulation step was fixed to $\tau = 1\,\mathrm{second}$, the position and velocity coordinates were in (m) and (m/step), respectively. The total number of time instants was $K = 20$.

The actual transition of the source followed the linear model in (3) with the transition function and covariance matrix set to have a nearly constant velocity movement according to

$$\mathbf{A} = \left[\begin{array}{cc} \mathbf{I}_3 & \tau\,\mathbf{I}_3 \\ \mathbf{0}_3 & \mathbf{I}_3 \end{array}\right], \quad \mathbf{Q} = \left[\begin{array}{cc} \frac{\tau^3}{3}\mathbf{Q}_{\mathrm{a}} & \frac{\tau^2}{2}\mathbf{Q}_{\mathrm{a}} \\ \frac{\tau^2}{2}\mathbf{Q}_{\mathrm{a}} & \tau\,\mathbf{Q}_{\mathrm{a}} \end{array}\right], \quad (75)$$

where $\mathbf{Q}_{\mathrm{a}}$ is a diagonal matrix containing the variances of the change in accelerations, i.e., $\mathbf{Q}_{\mathrm{a}} = \mathrm{diag}\left(\sigma_{\mathrm{a,x}}^2, \sigma_{\mathrm{a,y}}^2, \sigma_{\mathrm{a,z}}^2\right)$, with $\sigma_{\mathrm{a,x}}^2 = \sigma_{\mathrm{a,y}}^2 = \gamma_{\mathrm{t}}\,0.03^2\,(\mathrm{m}^2/\mathrm{step}^6)$, $\gamma_{\mathrm{t}} = 1$, and $\sigma_{\mathrm{a,z}}^2 = 0$. Instead, for the tracking estimator, we considered alternatively $\gamma_{\mathrm{t}} = 1$ and $\gamma_{\mathrm{t}} = 10$, that represented the possibility to work with transition model parameters that are the same of those used for the actual target trajectory (transition parameter match - TM_0) or not (transition parameter mismatch - TM_1), respectively. The measurements were generated using the model described by (4)-(6), where the noise standard deviation was set to $\sigma_\eta = \sigma \cdot (1 + \gamma_{\mathrm{m}})$ with $\sigma = 20°$ (if not otherwise indicated) and where $\gamma_{\mathrm{m}} = 0$ (i.e., $\sigma_\eta = 20°$) and $\gamma_{\mathrm{m}} = 1$ (i.e., $\sigma_\eta = 40°$) denote a model parameter match (measurement parameter match - MM_0) or mismatch (measurement parameter match - MM_1), respectively.

The EKF and the particles were initialized according to

$$\mathbf{m}_0 = \mathbf{s}_{m,0} = \mathcal{N}\left(\mathbf{s}_0, \mathbf{P}_0\right), \quad (76)$$

$$\mathbf{P}_0 = \mathrm{diag}\left(0.5^2, 0.5^2, 0.01^2, \frac{v_{\mathrm{x},0}^2}{10}, \frac{v_{\mathrm{y},0}^2}{10}, \frac{v_{\mathrm{z},0}^2}{100}\right), \quad (77)$$

if not otherwise indicated. In the PF method, we exploited the multinomial resampling strategy [54]. For the likelihood IS, we set $\mathbf{P}_{\mathrm{ML},k} = \mathbf{P}_0, \forall k$.

For the MLE when estimating the source position, we used a scatter search algorithm implemented in MATLAB software (GlobalSearch command) to find a global minimum [58].
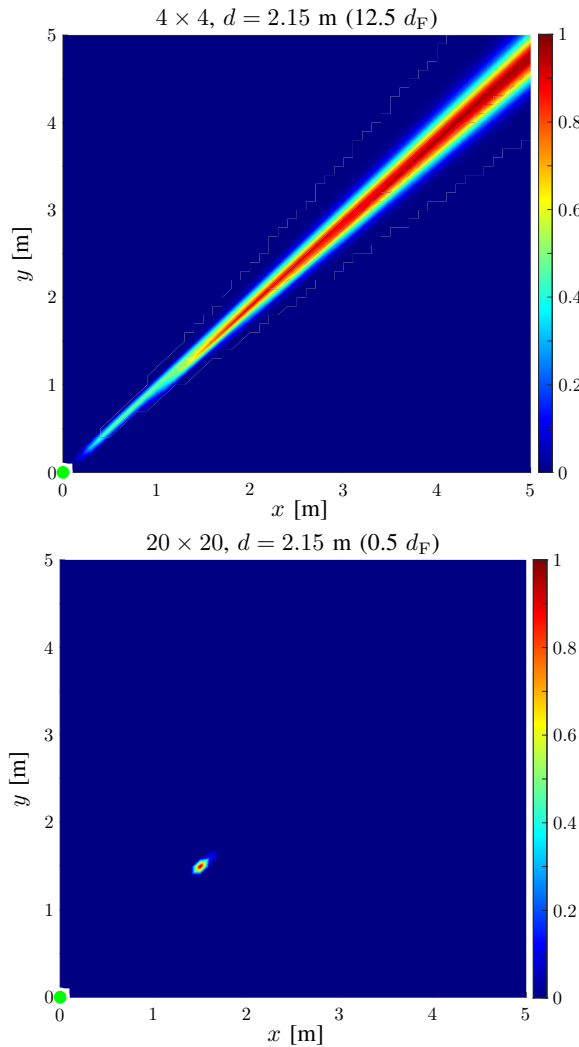
Fig. 5. Normalized LF for planar arrays with 4×4 (top) and 20×20 (bottom) antennas on the $YZ-$ plane, with $\sigma_\eta = 20°$. The receiver and target locations were in $[0, 0, 1]$ (indicated as green markers) and in $[1.51, 1.51, 1]$.

B. Numerical results

1) Likelihood function: We first investigate the LF shape considering the observation model in (6) and a target located inside and outside the Fresnel region, delimited by d_F. To that end, we considered a $5 \times 5\,\text{m}^2$ grid of points equally spaced with a step of $0.1\,\text{m}$ corresponding to the state $\mathbf{s}_k^i$, with i being the index of the ith grid point and k the time instant. For each test position, we computed the LF related to the actual state.

Fig. 5 shows the normalized LF for 4×4 and 20×20 arrays. The target was located at a distance of $d = 2.15\,\text{m}$ from the array that corresponds to $0.5\,d_F$ for the 20×20 array and $12.5\,d_F$ for the 4×4 array. Note that the LF is peaky and focused on the target's position when a large antenna array is used as the target falls in its near–field region, whereas it becomes less and less sharp and with ambiguities when exiting the Fresnel region because the effect of the CoA tends to vanish. Nevertheless, as demonstrated in Sec III, there is no variation in the performance of the angle estimation when moving from the near–field to the far–field region, as also evident from the sector shape in Fig. 5 (top).
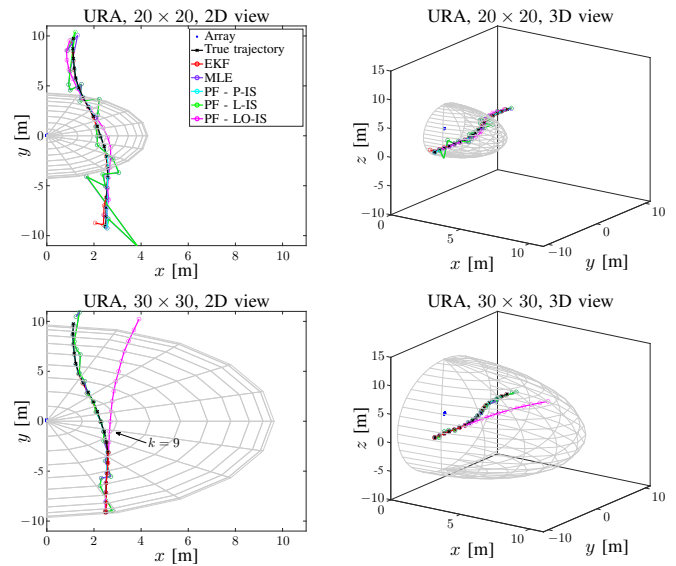

Fig. 6. Example of estimated trajectories for different approaches and array sizes. Top: URA with $N = 20 \times 20$ antennas, TM_0, MM_0; Bottom: URA with $N = 30 \times 30$ antennas, TM_0, MM_0. The array reference location is in $[0, 0, 1]$ and is lying in the YZ plane. (P-IS) indicates the PF with prior IS, (LO-IS) is the PF with linearised optimal IS and (L-IS) is the PF with likelihood IS.

2) Tracking scenarios: In Fig. 6, we present the estimated trajectories for two different arrays with $N = 20 \times 20$ (top) and 30×30 (bottom). The Fresnel region is displayed as a grey sphere, whereas the actual trajectory of the source with black line with cross markers at each time step. The estimated trajectories are depicted with different colors according to the tracking approach and to the legend. The parameters used in the models for generating the data are the same used by the estimators, i.e., perfect parameter match ($\gamma_t = 1$, $\gamma_m = 0$). When $N = 20 \times 20$, the initial and final points of the source trajectory were outside the Fresnel region. Consequently, from the analysis in Sec. III-B, in these areas, measurements are less informative about the source state and larger errors were made in the trajectory estimation, especially by those estimators mainly based on the information retrieved from LF, i.e., the PF with likelihood IS and the MLE. On the contrary, when operating in the near–field region, the tracking performance significantly improves. We notice that the PF with linearised optimal IS (namely PF - LO-IS in the figures) is less robust and accurate in estimating the trajectory than the other PF methods. In contrast to the prior IS (PF - P-IS), the particle propagation depends both on the transition and measurement densities, which are not always in perfect accordance with each other. This is evident when the LF becomes extremely peaky (i.e., when the source is very close to the array or with a large number of measurements). Then, it is very likely that particles are not propagated in regions of large probability masses because the likelihood is not overlapped with regions of high transition density [57].

We explain this effect through Fig 7 where we represent the locations of the weighted particles with linearised optimal and prior IS for the measurement update at time instant $k = 9$ and time update at $k = 8$ (prediction for $k = 9$). The weighted
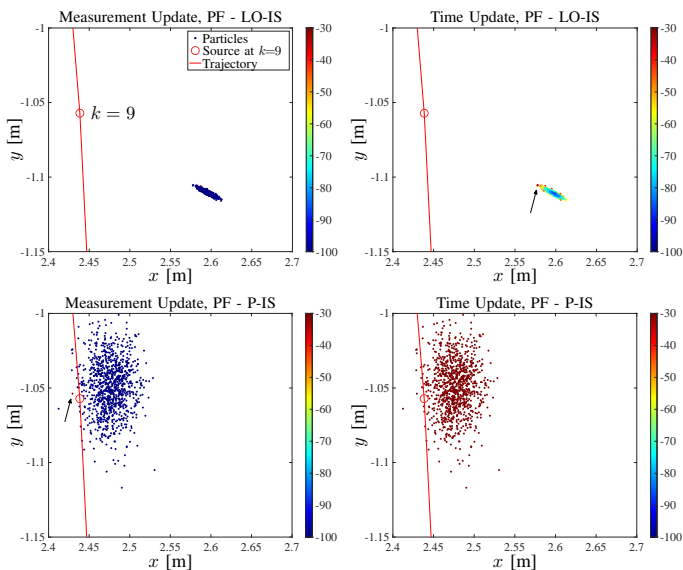
Fig. 7. Particles and weights for a PF with linearised optimal IS (top) and for prior IS (bottom) for a URA with 30×30 antennas. Left: Measurement update at $k = 9$. Right: Time update at $k = 8$ (prediction to $k = 9$).

Fig. 8. An array with 30×30 antennas is used for source tracking under transition model mismatches (i.e., the source follows a zigzag trajectory that does not correspond with the model in (75)). The transition model considers $\gamma_{\mathsf{t}} = 1$ (left) and $\gamma_{\mathsf{t}} = 10^3$ (right), The EKF and PF with linearised optimal IS are not reported in the figure because they experience large tracking error in presence of such mismatch.

particles are reported as circled markers with a color whose numerical value is reported in dB in the adjacent colorbar. The plots are snapshots of what happens when passing from time instant $k = 8$ to $k = 9$, i.e., when the source is in front of the array (at the same y coordinate) as also represented in Fig. 6. We have chosen this specific time instant because it corresponds to the time when the estimated track of PF with linearised optimal IS diverges from the actual source track in Fig. 6. During the measurement update, the predictive weights are modified by the likelihood as in (63). In Fig 7-(top, left), the particles of the PF linearised optimal IS are propagated in a region where the LF is not informative. Thus, in this example, all the weights of the particles have a small spatial dispersion, and very low weights of about $-100\,\mathrm{dB}$ corresponding to the LF tails. Conversely, in the prior IS case of Fig 7-(bottom, left), the likelihood peak can be more easily caught because with the time update, the algorithm sets all the weights to $1/M$ ($-30\,\mathrm{dB}$, with $M = 1000$) and propagates them only using the transition model with a bigger spatial dispersion. In this case, we can see that few particles, indicated with an arrow in the plot, intercept the peak of the LF.

The problem of the optimal IS can be partially overcome by increasing the uncertainty on the measurement model. This is equivalent to performing a *roughening* operation, i.e., a spreading of the LF by increasing its variance [59].

In Fig. 8, we show a different target trajectory with abrupt changes in direction. Indeed, rapid variations of the trajectory are more challenging from a tracking perspective [60]. This corresponds to a transition model mismatch, which means that the transition function is not accurate in predicting the new state $\mathbf{s}_k$. Consequently, in this case, a bigger transition covariance matrix is beneficial for PF with prior IS to increase the probability of propagating particles in informative regions. In fact, the target trajectory is not well described by the model in (75) and, thus, a larger uncertainty leads to smaller inertia
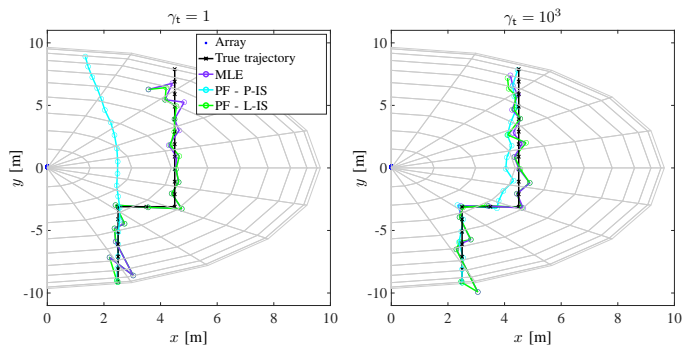
in the estimation process and to better results. This is not true for the EKF and PF with linearised optimal IS because in these algorithms the linearisation of the observation model requires a transition model that matches the behavior of the actual trajectory, as also evaluated in Fig. 11.

3) Tracking performance: The previous results were obtained by considering a single realization to get a qualitative idea about the performance behavior of the investigated tracking algorithms and of their robustness. Now, considering the same target trajectory shown in Fig. 6, we perform a performance comparison through Monte Carlo simulations of many realizations of trajectories. As metrics for comparison, we consider the empirical cumulative distribution function (CDF) and the root mean square error (RMSE) defined as

$$\mathsf{CDF}\left(e_{\mathsf{th}}\right) = \frac{1}{N_{\mathsf{mc}}\,K} \sum_{\ell=1}^{N_{\mathsf{mc}}} \sum_{k=1}^{K} \mathbf{1}\left(e_{\ell,k} \leq e_{\mathsf{th}}\right), \qquad (78)$$

$$\mathsf{RMSE}_k = \sqrt{\frac{1}{N_{\mathsf{mc}}} \sum_{\ell=1}^{N_{\mathsf{mc}}} e_{\ell,k}^2}, \qquad (79)$$

where the Monte Carlo cycles were fixed to $N_{\mathsf{mc}} = 100$, $\mathbf{1}\left(\cdot\right)$ is equal to one if its logical argument is true, otherwise it is zero, $e_{\ell,k} = \|\hat{\mathbf{p}}_{\ell,k} - \mathbf{p}_k\|$ is the localization error, $\hat{\mathbf{p}}_{\ell,k}$ is the estimated target position at time instant k for the ℓth Monte Carlo run, and e_{th} is a threshold for the localization error.

Figure 9-10 depicts the RMSE (top) and empirical CDF (bottom) obtained for $N = 20 \times 20$ and $N = 30 \times 30$, respectively, for $\sigma_\eta = 20°$ when the parameters match both in the measurement and transition models (i.e., TM_0 and MM_0). The CDF is shown as a function of the localization error, whereas the RMSE is studied as a function of time. The trace of the square root of the posterior Cramér-Rao Lower Bound (CRLB), namely $\sqrt{\mathsf{P\text{-}CRLB}}$, is also shown as performance benchmark. As intuitively predictable, the likelihood IS performs better for 30×30 than for the 20×20 thanks to the more peaky LF, as the target is always located within the near–field region of the receiver. On the other hand, the PF with linearised optimal IS has lower performance, especially for the 30×30 array. The EKF also allows to attain reliable
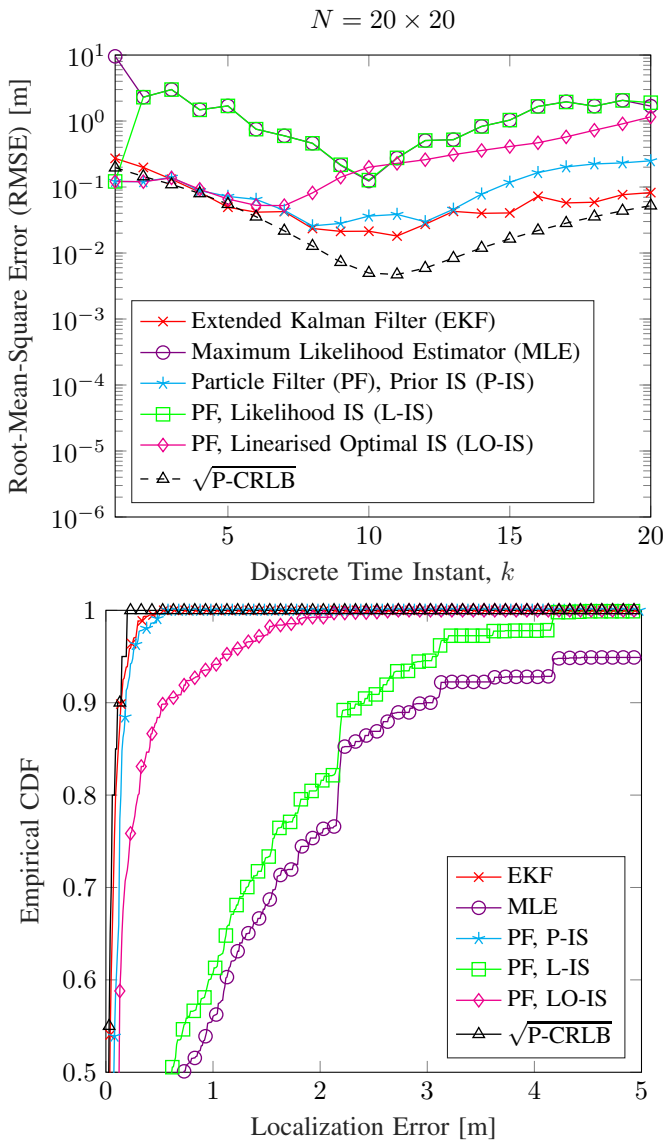
Fig. 9. RMSE (top) and Empirical CDF (bottom) vs. Localization error in meters for different estimators and by considering a URA with $N = 20 \times 20$ antennas, respectively. The measurement noise variance is set to $\sigma_\eta = 20°$.
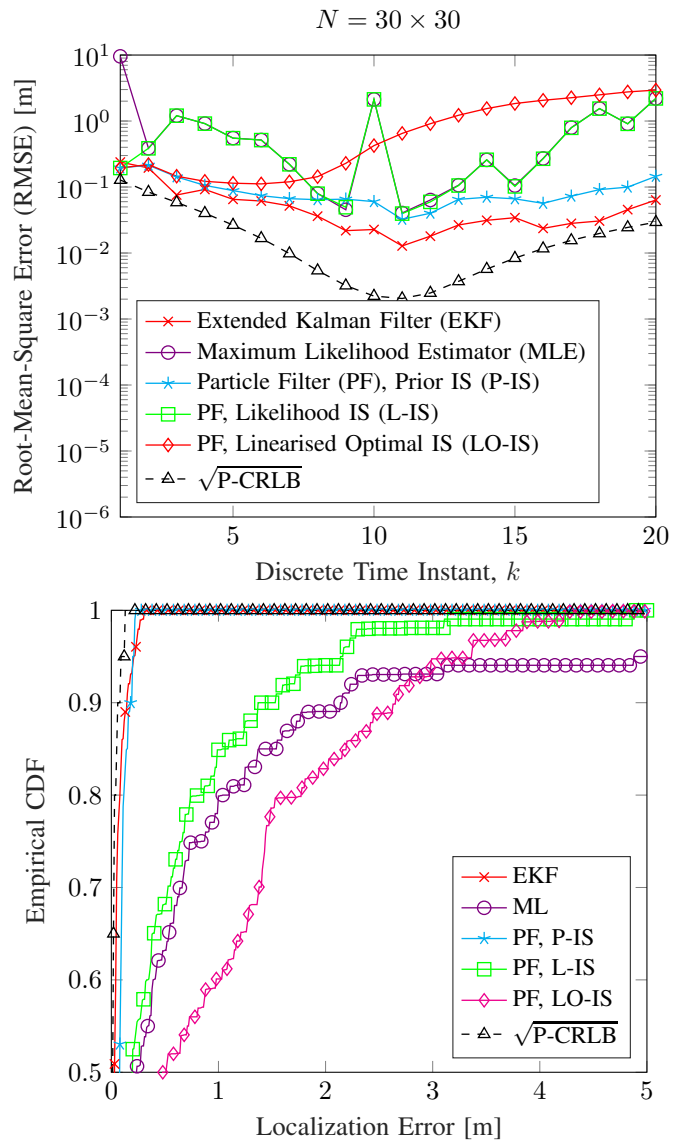

Fig. 10. RMSE (top) and Empirical CDF (bottom) vs. Localization error in meters for different estimators and by considering a URA with $N = 30 \times 30$ antennas, respectively. The measurement noise variance is set to $\sigma_\eta = 20°$.

performance despite its low complexity, provided that it is well initialized. The RMSE achieves its minimum value when the source is inside the Fresnel region and at the minimum distance from the antenna array (i.e., when $k \approx 10$).

We also evaluated the impact of parameter mismatches for the PF, considering a 20×20 array. The results in Fig. 11 suggest that the prior IS is robust to model mismatches, as the red curves exhibit similar behaviors. In particular, with large variances in the models, the system was more robust to trajectory variations and, consequently, it could track the target with a slightly improved accuracy. On the flip side, the optimal IS with linearized likelihood was more sensitive to the accuracy of the model. In this case, the joint variations in the transition parameters together with the peaky likelihood dramatically affected the performance. We observed performance improvement by introducing a measurement parameter mismatch (TM_0, MM_1).

Finally, the results of the performance as a function of the number of particles are presented in Fig. 12. They show that $M = 1000$ is a good tradeoff in terms of obtained accuracy.

4) Computational Complexity Analysis: We finally provide a brief discussion about the computational complexity of the algorithms described in Sec. IV.

Regarding the EKF, by considering that $N_s = 6 \ll N$, with N being the number of measurements, the total cost of the algorithm is mainly driven by the inversion of the innovation covariance matrix $\mathbf{S}_k$ and it goes as $\mathcal{O}\left(N^3\right)$.

Regarding the PF, the "Measurement Update", and "State Estimation" steps of Alg. 2 present the same computational complexity for all the approaches (i.e., prior, likelihood and linearised optimal IS). In particular, the complexity depends on the number of measurements and of particles M, and it is
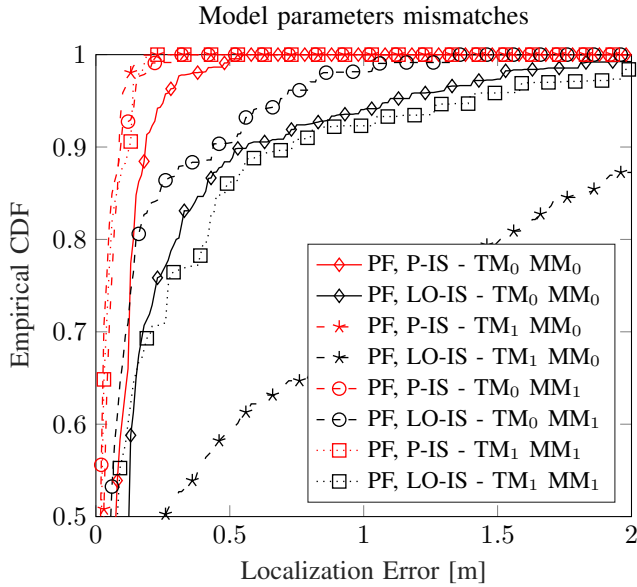
Fig. 11. Empirical CDF vs. Localization error in meters for particle filters using prior (red lines) and optimal (black lines) IS, by considering a rectangular array with $N = 20 \times 20$ antennas. Parameters mismatches are considered as described in Sec. V-A. Markers are plotted with a step of 10.
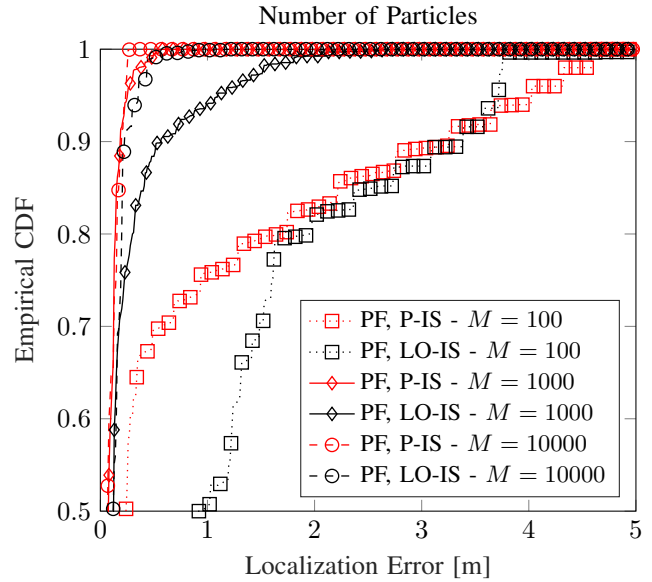

Fig. 12. Empirical CDF vs. Localization error in meters for particle filters using prior (red lines) and optimal (black lines) IS, by considering a rectangular array with $N = 20 \times 20$ antennas. The number of particles spans from 100 to 10000. Markers are plotted with a step of 10.

$\mathcal{O}\left(N^3 + M N^2\right)$ because of the inversion of the measurement covariance matrix $\mathbf{R}$ and of the likelihood derivation for each particle. For the "Time Update" in the PF, the cost depends on the chosen IS proposal as follows:

- *Prior* IS: the cost is $\mathcal{O}\left(M N_{\mathrm{s}}^2\right)$ driven by the instructions used for propagating particles;
- *Likelihood* IS: the cost is $\mathcal{O}\left(N_{\mathrm{s}}^3 + M N_{\mathrm{s}}^2 + c_2\left(N_{\mathrm{s}}, N\right)\right)$ depending on the MLE search (expressed with $c_2\left(N_{\mathrm{s}}, N\right)$), on the inversion of transition matrices ($\mathbf{P}_{\mathrm{ML}}^{-1}$ and $\mathbf{Q}^{-1}$), and on the computation of the transition and proposal densities;
- *Linearised Optimal* IS: the cost is $\mathcal{O}\left(M N_{\mathrm{s}}^3 + M N_{\mathrm{s}} N^2 + M N_{\mathrm{s}}^2 N\right)$, mainly depending on the computation and inversion of the covariance matrix $\mathbf{P}_{m,k}$ for each particle.

Consequently, by only comparing the PF approaches, the *prior IS* represents the less complex solution regardless the choice of the MLE implementation. Instead, the EKF presents the lowest complexity among all the other approaches because it does not involve the use of particles but it solves the tracking using a closed-form solution.

VI. CONCLUSIONS

In this paper, we investigated a tracking problem where a single array equipped with a co-located large number of antennas estimates the position of a source by exploiting the CoA information. First, we derived the theoretical bound on tracking estimation error, and we investigated the system ability to infer both angle and distance information (i.e., the position) when operating in the near–field region. This is enabled by processing the information of the electromagnetic wavefront curvature. The asymptotic analysis puts in evidence that the distance information tends to vanish when approaching the far–field region, which implies a scarce position estimation in the radial direction.

Second, we compared the performance of some state-of-the-art practical tracking algorithms to show the feasibility of accurate tracking using CoA information under different working conditions. Numerical results show that the performance of PF-based schemes is close to that of the theoretical bound, and, hence, sub-meter tracking accuracy can be obtained in the considered scenarios. Moreover, the comparison among different methods highlights that PF with prior IS is more robust to model mismatches and it is less computationally complex among the PF approaches.

Finally, our study indicates that it is possible to perform high accuracy tracking using one single antenna array and narrowband signals by exploiting the CoA in phase-difference measurements, provided that the target is within the near–field region of the antenna. In this setting, there is no need of accurate TOA estimation, which requires very large bandwidths and tight synchronization between the transmitter and the receiver.

APPENDIX A

We derive the expression for $\nabla_{\mathbf{s}} \Delta d_n$ where, for simplicity of notation, we omit the temporal index k. In particular, due to the fact that the derivatives with respect to the source velocity $\mathbf{v}_k$ are 0, we focus only on the source position. We can write

$$\nabla_{\mathbf{p}} \Delta d_n = \left[\sqrt{\mathrm{f}_n} - 1\right] \nabla_{\mathbf{p}} d + \frac{d \, \nabla_{\mathbf{p}} \, \mathrm{f}_n}{2 \sqrt{\mathrm{f}_n}}, \quad (80)$$

where $\nabla_{\mathbf{p}} \mathrm{f}_n$ is given by

$$\nabla_{\mathbf{p}} \mathrm{f}_n = -\frac{2 \, d_{n0}}{d}\left(\frac{d_{n0} \, \nabla_{\mathbf{p}} d}{d^2} + \nabla_{\mathbf{p}} g_n - \frac{g_n \, \nabla_{\mathbf{p}} \, d}{d}\right), \quad (81)$$

This article has been accepted for publication in IEEE Transactions on Signal Processing. This is the author's version which has not been fully edited and content may change prior to final publication. Citation information: DOI 10.1109/TSP.2021.3101696

IEEE TRANSACTIONS ON SIGNAL PROCESSING

15

with

$$\nabla_{\mathbf{p}} d = \left[\frac{\partial d}{\partial x}, \frac{\partial d}{\partial y}, \frac{\partial d}{\partial z} \right] = \left[\frac{x - x_0}{d}, \frac{y - y_0}{d}, \frac{z - z_0}{d} \right], \quad (82)$$

being the gradient of the distance with respect to the source position and where the gradient of the angular term g_n is

$$\nabla_{\mathbf{p}} g_n = \sin(\theta_{n0}) \left(\cos(\phi_{n0} - \phi) \cos(\theta) \nabla_{\mathbf{p}} \theta \right. \\ \left. + \sin(\theta) \sin(\phi_{n0} - \phi) \nabla_{\mathbf{p}} \phi \right) \\ - \cos(\theta_{n0}) \sin(\theta) \nabla_{\mathbf{p}} \theta, \quad (83)$$

with

$$\nabla_{\mathbf{p}} \theta = \left[\frac{\partial \theta}{\partial x}, \frac{\partial \theta}{\partial y}, \frac{\partial \theta}{\partial z} \right] \\ = \left[\frac{\cos(\phi) \cos(\theta)}{d}, \frac{\sin(\phi) \cos(\theta)}{d}, -\frac{\sin(\theta)}{d} \right], \quad (84)$$

$$\nabla_{\mathbf{p}} \phi = \left[\frac{\partial \phi}{\partial x}, \frac{\partial \phi}{\partial y}, \frac{\partial \phi}{\partial z} \right] = \left[-\frac{\sin(\phi)}{d \sin(\theta)}, \frac{\cos(\phi)}{d \sin(\theta)}, 0 \right]. \quad (85)$$

Now, it is easy to show that (25) holds. In fact, considering for example the x coordinate, we have

$$\frac{\partial \Delta d_n}{\partial x} = \frac{1}{d} \left\{ (x - x_0) \left[\sqrt{f_n} - 1 \right] - \frac{d_{n0}}{\sqrt{f_n}} \left(\frac{d_{n0}(x - x_0)}{d^2} \right. \right. \\ \left. \left. + d \frac{\partial g_n}{\partial x} - \frac{g_n(x - x_0)}{d} \right) \right\} \xrightarrow[d \gg d_F]{} 0. \quad (86)$$

Finally, the gradient of d_n with respect to the state is

$$\nabla_{\mathbf{p}} d_n = \frac{1}{d_n} \left[\Delta x_n \nabla_{\mathbf{p}} \Delta x_n + \Delta y_n \nabla_{\mathbf{p}} \Delta y_n + \Delta z_n \nabla_{\mathbf{p}} \Delta z_n \right], \quad (87)$$

where $\Delta x_n = x - x_n$, $\Delta y_n = y - y_n$, and $\Delta z_n = z - z_n$.

APPENDIX B

By substituting $\frac{\partial h_n}{\partial \xi} = \frac{2\pi}{\lambda} \frac{\partial \Delta d_n}{\partial \xi}$ and by omitting the temporal index for notation simplicity, we can reformulate (26) according to [61] as

$$\tilde{J}^{D}(\xi) = \frac{1}{\sigma_\eta^2} \sum_{n=0}^{N-1} \left(\frac{\partial h_n}{\partial \xi} \right)^2 = \frac{4\pi^2}{\lambda^2 \sigma_\eta^2} \sum_{n=0}^{N-1} \left(\frac{\partial \Delta d_n}{\partial \xi} \right)^2, \quad (88)$$

where the derivatives inside the summations of (88) depend on the actual significance of ξ and are given by

$$\frac{\partial \Delta d_n}{\partial d} = \sqrt{f_n} - 1 - \frac{d_{n0}}{d \sqrt{f_n}} \left(\frac{d_{n0}}{d} - g_n \right), \quad (89)$$

$$\frac{\partial \Delta d_n}{\partial \theta} = d \frac{\partial \sqrt{f_n}}{\partial \theta} = -\frac{d_{n0}}{\sqrt{f_n}} \frac{\partial g_n}{\partial \theta}, \quad (90)$$

$$\frac{\partial \Delta d_n}{\partial \phi} = d \frac{\partial \sqrt{f_n}}{\partial \phi} = -\frac{d_{n0}}{\sqrt{f_n}} \frac{\partial g_n}{\partial \phi}, \quad (91)$$

with f_n and g_n defined in (12) and (10), respectively, and with

$$\frac{\partial g_n}{\partial \theta} = \cos(\theta) \sin(\theta_{n0}) \cos(\phi_{n0} - \phi) - \sin(\theta) \cos(\theta_{n0}), \quad (92)$$

$$\frac{\partial g_n}{\partial \phi} = \sin(\phi_{n0} - \phi) \sin(\theta_{n0}) \sin(\theta). \quad (93)$$

By substituting f_n in (89)-(91) and squaring, we obtain

$$\left(\frac{\partial \Delta d_n}{\partial d} \right)^2 = \frac{\left(1 - \frac{g_n d_{n0}}{d} - \sqrt{1 + \frac{d_{n0}^2}{d^2} - 2 \frac{g_n d_{n0}}{d}} \right)^2}{1 + \frac{d_{n0}^2}{d^2} - 2 \frac{g_n d_{n0}}{d}}, \quad (94)$$

$$\left(\frac{\partial \Delta d_n}{\partial \theta} \right)^2 = \frac{d_{n0}^2}{1 + \frac{d_{n0}^2}{d^2} - 2 \frac{g_n d_{n0}}{d}} \left(\frac{\partial g_n}{\partial \theta} \right)^2, \quad (95)$$

$$\left(\frac{\partial \Delta d_n}{\partial \phi} \right)^2 = \frac{d_{n0}^2}{1 + \frac{d_{n0}^2}{d^2} - 2 \frac{g_n d_{n0}}{d}} \left(\frac{\partial g_n}{\partial \phi} \right)^2. \quad (96)$$

By injecting the expressions above into (88), we obtain (28).

APPENDIX C

In this case, given the Assumption 1 and 2, we can write (28)-(29) as

$$\tilde{J}^{D}(d) = \frac{4\pi^2}{\lambda^2 \sigma_\eta^2} \sum_{n=0}^{N-1} \frac{8 d^2 + D^2 - 4 d \sqrt{4 d^2 + D^2}}{4 d^2 + D^2}, \quad (97)$$

$$\tilde{J}^{D}(\theta) = \frac{\pi^2}{\lambda^2 \sigma_\eta^2} \frac{D^2}{1 + \frac{D^2}{4 d^2}} \sum_{n=0}^{N-1} \left(\cos \left(2 \pi \frac{n}{N} \right) \right)^2, \quad (98)$$

$$\tilde{J}^{D}(\phi) = \frac{\pi^2}{\lambda^2 \sigma_\eta^2} \frac{D^2}{1 + \frac{D^2}{4 d^2}} \sum_{n=0}^{N-1} \left(\sin \left(2 \pi \frac{n}{N} \right) \right)^2, \quad (99)$$

where we have exploited the following relationships

$$\left(\frac{\partial g_n}{\partial \theta} \right)^2 = (\cos \theta_{n0})^2 = \left(\cos \left(2 \pi \frac{n}{N} \right) \right)^2, \quad (100)$$

$$\left(\frac{\partial g_n}{\partial \phi} \right)^2 = (\sin \theta_{n0})^2 = \left(\sin \left(2 \pi \frac{n}{N} \right) \right)^2, \quad (101)$$

and

$$\sum_{n=0}^{N-1} \left(\cos \left(2 \pi \frac{n}{N} \right) \right)^2 = \sum_{n=0}^{N-1} \left(\sin \left(2 \pi \frac{n}{N} \right) \right)^2 = \frac{N}{2}. \quad (102)$$

Then, (97)-(99) can be further simplified as in (36)-(37).

REFERENCES

[1] M. Z. Win, Y. Shen, and W. Dai, "A theoretical foundation of network localization and navigation," *Proc. IEEE*, vol. 106, no. 7, pp. 1136–1165, Jul. 2018, special issue on *Foundations and Trends in Localization Technologies*.

[2] D. Dardari, P. Closas, and P. M. Djurić, "Indoor tracking: Theory, methods, and technologies," *IEEE Trans. Veh. Technol.*, vol. 64, no. 4, pp. 1263–1278, Apr. 2015.

[3] H. Wymeersch, J. Lien, and M. Z. Win, "Cooperative localization in wireless networks," *Proc. IEEE*, vol. 97, no. 2, pp. 427–450, 2009.

[4] M. Z. Win *et al.*, "Network localization and navigation via cooperation," *IEEE Commun. Mag.*, vol. 49, no. 5, pp. 56–62, 2011.

[5] D. Dardari *et al.*, "Ranging with ultrawide bandwidth signals in multipath environments," *Proc. IEEE*, vol. 97, no. 2, pp. 404–426, 2009.

[6] H. Durrant-Whyte and T. Bailey, "Simultaneous localization and mapping: Part I," *IEEE Robot. Automat. Mag.*, vol. 13, no. 2, pp. 99–110, 2006.

[7] F. Guidi and D. Dardari, "Radio positioning with EM processing of the spherical wavefront," *IEEE Trans. Wireless Commun.*, vol. 20, no. 6, pp. 3571–3586, 2021.

[8] D. Dardari and N. Decarli, "Holographic communication using intelligent surfaces," *IEEE Commun. Mag.*, vol. 59, no. 6, pp. 35–41, June 2021.

This article has been accepted for publication in IEEE Transactions on Signal Processing. This article is the author's version which has not been fully edited and content may change prior to final publication. Citation information: DOI 10.1109/TSP.2021.3101696

IEEE TRANSACTIONS ON SIGNAL PROCESSING

16

[9] C. De Lima *et al.*, "Convergent communication, sensing and localization in 6G systems: An overview of technologies, opportunities and challenges," *IEEE Access*, 2021.

[10] A. Fascista *et al.*, "Millimeter-wave downlink positioning with a single-antenna receiver," *IEEE Trans. Wireless Commun.*, vol. 18, no. 9, pp. 4479–4490, 2019.

[11] F. Guidi *et al.*, "Indoor environment-adaptive mapping with beamsteering massive arrays," *IEEE Trans. Veh. Technol.*, vol. 67, no. 10, pp. 10 139–10 143, Oct. 2018.

[12] A. Guerra, F. Guidi, and D. Dardari, "Single anchor localization and orientation performance limits using massive arrays: MIMO vs. beamforming," *IEEE Trans. Wireless Commun.*, vol. 17, no. 8, pp. 5241–5255, 2018.

[13] A. Elzanaty *et al.*, "Towards 6G Holographic Localization: Enabling Technologies and Perspectives," *arXiv preprint arXiv:2103.12415*, 2021.

[14] N. Garcia *et al.*, "Direct localization for massive MIMO," *IEEE Trans. Signal Process.*, vol. 65, no. 10, pp. 2475–2487, 2017.

[15] Y. Wang, Y. Wu, and Y. Shen, "Joint spatiotemporal multipath mitigation in large-scale array localization," *IEEE Trans. Signal Process.*, vol. 67, no. 3, pp. 783–797, Feb 2019.

[16] H. Wymeersch, "A Fisher information analysis of joint localization and synchronization in near field," in *Proc. IEEE Int. Conf. Commun. Workshops (ICC Workshops)*, 2020, pp. 1–6.

[17] S. Zhang *et al.*, "Spherical wave positioning based on curvature of arrival by an antenna array," *IEEE Wireless Commun. Lett.*, vol. 8, no. 2, pp. 504–507, Apr. 2019.

[18] A. Elzanaty *et al.*, "Reconfigurable intelligent surfaces for localization: Position and orientation error bounds," *in Publication, IEEE Trans. Signal Process.*, 2021.

[19] N. Hadaschik, B. Sackenreuter, and M. Faßbinder, "Direct multi-array and multi-tone positioning," in *Proc. IEEE Int. Conf. Commun. Workshop*, May 2017, pp. 1067–1072.

[20] M. N. E. Korso *et al.*, "Deterministic performance bounds on the mean square error for near field source localization," *IEEE Trans. Signal Process.*, vol. 61, no. 4, pp. 871–877, Feb. 2013.

[21] J.-P. Le Cadre, "Performance analysis of wavefront curvature methods for range estimation of a moving source," *IEEE Trans. Aerosp. Electron. Syst.*, vol. 31, no. 3, pp. 1082–1103, 1995.

[22] B. Friedlander, "Localization of signals in the near-field of an antenna array," *IEEE Trans. Signal Process.*, vol. 67, no. 15, pp. 3885–3893, 2019.

[23] A. Manikas, Y. I. Kamil, and M. Willerton, "Source localization using sparse large aperture arrays," *IEEE Trans. Signal Process.*, vol. 60, no. 12, pp. 6617–6629, 2012.

[24] N. Vukmirović *et al.*, "Direct wideband coherent localization by distributed antenna arrays," *Sensors*, vol. 19, no. 20, p. 4582, 2019.

[25] ——, "Position estimation with a millimeter-wave massive MIMO system based on distributed steerable phased antenna arrays," *EURASIP J. Adv. Signal Process.*, vol. 2018, no. 1, pp. 1–17, 2018.

[26] E. Grosicki, K. Abed-Meraim, and Y. Hua, "A weighted linear prediction method for near-field source localization," *IEEE Trans. Signal Process.*, vol. 53, no. 10, pp. 3651–3660, 2005.

[27] J.-F. Chen, X.-L. Zhu, and X.-D. Zhang, "A new algorithm for joint range-DOA-frequency estimation of near-field sources," *EURASIP J. Adv. Signal Process.*, vol. 2004, no. 3, pp. 1–7, 2004.

[28] Y.-D. Huang and M. Barkat, "Near-field multiple source localization by passive sensor array," *IEEE Trans. Antennas Propag.*, vol. 39, no. 7, pp. 968–975, 1991.

[29] M. N. E. Korso *et al.*, "Sequential estimation of the range and the bearing using the Zero-Forcing Music approach," in *Proc. 17th European Signal Process. Conf. (EUSIPCO)*, Aug. 2009, pp. 1404–1408.

[30] B. G. Ferguson and R. J. Wyber, "Wavefront curvature passive ranging in a temporally varying sound propagation medium," in *Proc. MTS/IEEE Oceans. An Ocean Odyssey*, vol. 4, 2001, pp. 2359–2365 vol.4.

[31] Y. I. Kamil and A. Manikas, "Multisource spatiotemporal tracking using sparse large aperture arrays," *IEEE Trans. Aerosp. Electron. Syst.*, vol. 53, no. 2, pp. 837–853, 2017.

[32] Z. Tang and A. Manikas, "Direction-of-arrival tracking of multiple fast-moving sources in antenna array based access networks," in *Proc. IEEE Int. Conf. Commun. (ICC)*, 2020, pp. 1–6.

[33] E. Venieris and A. Manikas, "Near-far field multipath spatial-temporal localisation," in *IEEE Int. Conf. Commun. Workshops (ICC)*, 2017, pp. 1049–1054.

[34] P. Nepa *et al.*, "Technologies for near-field focused microwave antennas," *Int. J. Antennas Propag.*, vol. 2017, 2017.

[35] A. Mudonhi *et al.*, "RIS-enabled mmwave channel sounding based on electronically reconfigurable transmitarrays," in *Proc. 15th European Conf. Antennas Propag. (EuCAP)*. IEEE, 2021, pp. 1–5.

[36] L. Di Palma *et al.*, "Circularly-polarized reconfigurable transmitarray in Ka-band with beam scanning and polarization switching capabilities," *IEEE Trans. Antennas Propag.*, vol. 65, no. 2, pp. 529–540, 2016.

[37] S. Hu, F. Rusek, and O. Edfors, "Beyond massive MIMO: The potential of positioning with large intelligent surfaces," *IEEE Trans. Signal Processing*, vol. 66, no. 7, pp. 1761–1774, Apr. 2018.

[38] E. Björnson *et al.*, "Reconfigurable intelligent surfaces: A signal processing perspective with wireless applications," *arXiv preprint arXiv:2102.00742*, 2021.

[39] C. Hue, J.-P. Le Cadre, and P. Perez, "Posterior Cramer-Rao bounds for multi-target tracking," *IEEE Trans. Aerosp. Electron. Syst. .*, vol. 42, no. 1, pp. 37–49, 2006.

[40] M. N. El Korso *et al.*, "Conditional and unconditional Cramér–Rao bounds for near-field source localization," *IEEE Trans. Signal Process.*, vol. 58, no. 5, pp. 2901–2907, 2010.

[41] S. Zhang *et al.*, "Spherical wave positioning based on curvature of arrival by an antenna array," *IEEE Wireless Commun. Lett.*, vol. 8, no. 2, pp. 504–507, Apr. 2019.

[42] A. D. J. Torres *et al.*, "Cramér-Rao Bounds for Near-Field Localization," *arXiv preprint arXiv:2104.14825*, 2021.

[43] E. Björnson *et al.*, "Reconfigurable Intelligent Surfaces: A Signal Processing Perspective With Wireless Applications," *arXiv preprint arXiv:2102.00742*, 2021.

[44] C. Balanis, *Antenna Theory*, 3rd ed. Wiley, 2005.

[45] S. Särkkä, *Bayesian filtering and smoothing*. Cambridge University Press, 2013, vol. 3.

[46] P. Tichavsky, C. H. Muravchik, and A. Nehorai, "Posterior Cramér-Rao bounds for discrete-time nonlinear filtering," *IEEE Trans. Signal Process.*, vol. 46, no. 5, pp. 1386–1396, 1998.

[47] T. Bréhard and J.-P. Le Cadre, "Closed-form posterior Cramér-Ra bounds for bearings-only tracking," *IEEE Trans. Aerosp. Electron. Syst.*, vol. 42, no. 4, pp. 1198–1223, 2006.

[48] N. Bergman, A. Doucet, and N. Gordon, "Optimal estimation and Cramér-Rao bounds for partial non-Gaussian state space models," *Annals of the Institute of Statistical Mathematics*, vol. 53, no. 1, pp. 97–112, 2001.

[49] C. Fritsche *et al.*, "A fresh look at Bayesian Cramér-Rao bounds for discrete-time nonlinear filtering," in *Proc. 17th Int. Conf. Information Fusion (FUSION)*, 2014, pp. 1–8.

[50] F. Koohifar, I. Guvenc, and M. L. Sichitiu, "Autonomous tracking of intermittent RF source using a UAV swarm," *IEEE Access*, vol. 6, pp. 15 884–15 897, 2018.

[51] S. M. Kay, *Fundamentals of statistical signal processing*. Prentice Hall PTR, 1993.

[52] P. M. Djurić *et al.*, "Particle filtering," *IEEE Signal Process. Mag.*, vol. 20, no. 5, pp. 19–38, 2003.

[53] P. M. Djurić, M. Vemula, and M. F. Bugallo, "Target tracking by particle filtering in binary sensor networks," *IEEE Trans. Signal Process.*, vol. 56, no. 6, pp. 2229–2238, 2008.

[54] T. Li, M. Bolic, and P. M. Djurić, "Resampling methods for particle filtering: classification, implementation, and strategies," *IEEE Signal Process. Mag.*, vol. 32, no. 3, pp. 70–86, 2015.

[55] A. Doucet, S. Godsill, and C. Andrieu, "On sequential Monte Carlo sampling methods for Bayesian filtering," *Stat. Comput.*, vol. 10, no. 3, pp. 197–208, 2000.

[56] F. Gustafsson, "Particle filter theory and practice with positioning applications," *IEEE Aerosp. Electron. Sys. Mag.*, vol. 25, no. 7, pp. 53–82, 2010.

[57] P. Bunch and S. Godsill, "Particle filtering with progressive Gaussian approximations to the optimal importance density," in *Proc. of 5th IEEE Int. Workshop Comput. Adv. Multi-Sensor Adapt. Process. (CAMSAP)*. IEEE, 2013, pp. 360–363.

[58] Z. Ugray *et al.*, "Scatter search and local NLP solvers: A multistart framework for global optimization," *INFORMS J. Comput.*, vol. 19, no. 3, pp. 328–340, 2007.

[59] F. Boccardi *et al.*, "Five disruptive technology directions for 5G," *IEEE Commun. Mag.*, vol. 52, no. 2, pp. 74–80, Feb. 2014.

[60] M. F. Bugallo, S. Xu, and P. M. Djurić, "Performance comparison of EKF and particle filtering methods for maneuvering targets," *Digital Signal Process.*, vol. 17, no. 4, pp. 774–786, 2007.

[61] D. B. Jourdan, D. Dardari, and M. Z. Win, "Position error bound for UWB localization in dense cluttered environments," *IEEE Trans. Aerosp. Electron. Syst.*, vol. 44, no. 2, pp. 613–628, 2008.